Effect of Polymer Structure and Chemistry on Viscosity Index, Thickening Efficiency, and Traction Coefficient of Lubricants

Pawan Panwar [1], Emily Schweissinger [2], Stefan Maier [2], Stefan Hilf [2], Sofia Sirak [2], and Ashlie Martini [1,*]

[1] Department of Mechanical Engineering, University of California Merced, 5200 N. Lake Road, Merced,

CA 95343, USA

[2] Evonik Operations GmbH, Kirschenallee, 64293 Darmstadt, Germany

* Correspondence: amartini@ucmerced.edu

Abstract

The chemistry and structure of base oil and polymer additive molecules in lubricants directly affect key performance metrics such as viscosity index, thickening efficiency, and traction coefficient. However, the relationship between molecular properties and these metrics is still not fully understood, inhibiting the design of new fluids with potentially improved performance. This study used molecular dynamics simulations to identify structure-property-function relationships for model lubricants consisting of branched and linear polymers with chemistries consistent with commercially available products. First, five fluids were formulated with different polymers but with the same kinematic viscosity at 100 °C. Then, the simulation-calculated Newtonian viscosities at 40 and 100 °C, viscosity index, thickening efficiency, and traction coefficient in full film lubrication at 40 °C were validated by direct comparison to experimental data. Next, the molecular origins of differences in the viscosity index, thickening efficiency, and traction coefficient between the fluids were investigated by calculating the multiple structural properties of the polymers in the simulations. Finally, the simulations were used to develop simple empirical models using the best subset linear regression analysis to rapidly predict viscosity index, thickening efficiency, and traction coefficient. The atomistic simulations and empirical models developed in this work can ultimately guide the design of new lubricants or additives.

1. Introduction

The viscosity of lubricants, an important fluid property that quantifies the resistance to flow, decreases rapidly as temperature increases [1–3]. This is a major concern for lubricants in applications that are operated at a wide range of temperatures; viscosity loss is a particular issue in applications with small oil reservoirs and compact heat exchangers. If the viscosity of a lubricant is too low at a high temperature, a thin lubricating film may no longer have adequate load carrying capacity, leading to asperity contact. The increase in asperity contact increases mechanical friction, which causes machine inefficiency, and surface wear which ultimately leads to component failure [4,5]. However, if a higher viscosity fluid is used to ensure a thick lubricating film of adequate load carrying capacity at high temperatures, that might lead to a poor efficiency at low temperatures due to increase in viscous friction. Therefore, it is desirable for lubricant viscosity to decrease as slowly as possible with increasing temperature. Viscosity index (VI) is the most used metric to quantify the viscosity–temperature relationship of a lubricant, as defined by ASTM D2270 standard [6]. Another important metric is thickening efficiency (TE) that describes the amount of polymer (that is, polymer treat rate) that required in a lubricant formulation to reach either a desired kinematic viscosity or dynamic viscosity at a temperature or 100°C [7]. It is desirable to use as little polymer as possible to achieve good temperature-viscosity behavior, i.e. high TE and VI [8].

Like viscosity, the traction (or viscous friction) is a complex but important pressure- and shear-dependent fluid property that quantifies the force resistance to shearing effects within an (elasto)hydrodynamic lubrication (EHL) contact. Traction is due entirely to the fluid properties and so is not to be confused with contact friction, which is associated with surface interactions. The traction response is dominated by the shear behavior of the lubricant in the central high contact pressure region of a contact and this property of a fluid is quantified by a parameter known as traction coefficient (TC). Generally, the traction coefficient increases with increasing slide-to-roll ratio [9–11] and contact pressure [9,10], and decreasing entrainment speed [10,12–14] and decreasing temperature [9,10]. An axial piston pump and a radial piston motor efficiency tests on five commercial ISO 46 viscosity grade fluids revealed that a low traction fluid decreased the low-speed torque losses as much as by 50% [14]. Similar findings were presented by Michael at el. [13] in which low traction coefficient fluid found to improved overall low-speed efficiency of a hydraulic motor by 5-16% via transitioning out of the boundary lubrication region at a lower Stribeck/Hersey number. As a result, low traction is preferable in hydraulic fluids [12–14] to decrease shearing forces and high traction is preferable in continuously variable transmissions fluids to avoid slippage while minimizing contact friction for energy efficiency [15–17]. Good traction characteristics in a lubricants are essential to achieving a balance between film thickness and resistance to shear to ensure both wear protection and energy efficiency [18].

Fluids are formulated with polymeric additives to maximum the viscosity-temperature and traction behavior [9,11,19–28]. Polymers in lubricants are used to serve range of purposes and perform their function through a variety of

mechanisms. The molecular weight of polymers ranges from 1-100 kg/mol [23–25]. Typical polymeric additives include polyalpha olefin (PAO), olefin copolymer (OCP), polyalkyl methacrylate (PAMA), polyisobutylene (PIB), styrene block copolymers (SBCP), and hydrogenated styrene–diene (HSD) [21,24,27,29]. All these polymers will increase viscosity relative to the viscosity of base oil but might have varying effects on the rate of change of viscosity with temperature for the same backbone length, depending on their composition and architecture. The mechanisms by which polymers perform their function depend on chemistry [30–32] and architecture [7,33,34] both of the polymer and the base oil.

The effect of molecular structure, architecture, and chemistry of polymeric additives on viscosity derived properties, e.g. VI and TE, have been explored using experimental methods [20,35–39] and molecular dynamics simulation tools [19,20,26,27,38,40–45]. The most often reported mechanism by which polymers increase VI of the fluids is coil expansion at higher temperature [46]. In fact, viscosity can be correlated to coil size quantified by the root-mean-square radius of gyration of the polymer [47,48]. While the coil expansion mechanism is widely accepted in the literature [7,21,23–25,49,50], it has been observed in some but not in all polymers both experimentally [2,38,51–53] and atomistic simulations [19,38,43,44]. For example, the coil size of some polymers, such as OCP and hydrogenated diene copolymers, remains constant or decreases with increasing temperature, whereas the coil size of polymers derived from esters, such as PAMA, increases with temperature [2,51–53]. Therefore, in general, hydrocarbon-based polymers such as OCP, PIB, PAO, SBCP, and HSD are known to provide better TE, while ester-based polymers such as PAMAs provide better VI [7,54]. More generally, it has been suggested that polymers that expand with temperature might increase VI more than those that do not expand [2]. For example, a block linear styrene–butadiene polymer configuration exhibited the least change in viscosity with temperature compared to alternating and random linear styrene–butadiene polymers, due to ability of the block structure to form smaller coils with more intramolecular interactions at lower temperatures and then expand at higher temperatures [44]. A molecular dynamics (MD) simulation study of PMA and OCP polymers revealed that the presence of electronegative atoms, such as the oxygen in methacrylate, is a key factor in determining if a polymer will expand or contract with temperature [43]. A similar finding was reported in a MD study where PAMA and star PAMA were found to have the highest VI due to polar backbones in contrast to the nonpolar backbones in linear OCP and hyperbranched HBPE polymers [38].

The molecular weight and molecular weight distribution of polymers are easily accessible but important parameters in characterizing polymers. TE was found to increase linearly with the percentage of molecular weight in the backbone of the polymer [21]. It has been also suggested that high molecular weight linear polymers provide better TE [21]. Higher ethylene content OCP polymers have better TE while PAMAs have higher VI [21]. Knowing that the distribution of molecular weight plays a significant role in characterizing rheological properties of fluids, various studies investigated the effect of chain shape (such as linear, comb, and star) [35,38,39,42,55]. An experimental study on polyethylene revealed that an increase of polymer molecular weight by intermolecular crosslinking was found to significantly improve TE which ultimately reduced their treat rate in the fluid [33,34]. On the other hand, another study [35] suggested that viscosity drastically decreased on addition of a hyperbranched polymer instead of a linear polymer. By narrowing the distribution of molecular weight of the polymer (that is the ratio of mass average molar mass to the number average molar mass) excellent TE can be achieved [21,56].

Polymer additives can increase [9,11] or decrease [11] the TC of a lubricant, depending on formulation. TC is typically characterized experimentally using a Mini-Traction-Machine (MTM), which is a ball-on-disk tribometer, at a range of operating conditions. Such studies showed that when the polyethylene polymer concentration was increased in mineral base oil from 0.0 to 2.0%, the TC increased [9]. In that study, a semi-empirical model was also developed to determine the effect of operating conditions such as pressure, temperature, and polymer concentration on TC [9]. The model showed that TC is a function of natural logarithm of shear rate [9]. Experimental study showed that higher naphthenic carbon content of mineral oil correlates to higher shear resistance [57], some compounds with a gem-dimethyl structure showed higher coefficient of traction than others [58], and the maximum TC of aliphatic hydrocarbon oils increased with increasing degree of branching [59]. An investigation reported that the flow activation volumes, which was calculated by applying Eyring's hole theory, for viscous flow of 26 lubricating oils was linearly related to the maximum TC [60]. Another study [61,62] investigated 37 molecular structures of traction base fluids of various chemical groups (naphthenes, aromatics, paraffins, ethers, ketones, alcohols, chlorides, and amides) to understand the factors influencing traction and recommended that high molecular stiffness, large size, short alkylene chain length, high melting point, low molecular polarity for the molecule structure to provide a high TC. Polar compounds have a high viscosity due to the molecular interaction force under semi-static conditions but have a low TC due to the repulsion of negative charges under traction conditions (that is, high pressure and high shear rate) [63]. Molecular mechanics modelling [64]

qualitatively correlated the TC of ester compounds to the angle of rotation around the C-C bond between ester groups and the potential energy. Other simulations showed that compounds with saturated rings have a high TC and molecular stiffness governs traction properties [65]. A molecular dynamics (MD) study suggested that a polycyclic compounds with ester functional groups are preferable for reducing traction [66] due to slip between rings. Although such studies indicate that simulations can be used to understanding the molecular mechanisms TC, the few studies [66–71] that have been performed either focused on method development or understanding TC only for very small molecules.

These studies demonstrate that there is a wide range of functionality and behavior of polymers in lubricant formulations. The structure and chemistry of the polymers vary depending on their purpose and affect the mechanisms by which they function. However, the correlations between structure/chemistry and lubricant function are still poorly understood. In this context, the goal of this project was to characterize the effect of polymer chemistry/structure on VI, TE, and TC. To achieve this goal, we used MD simulations of five commercially relevant polymer-base oil formulations. The simulations were used to obtain viscosity using standard methods at 40 and 100 °C, and VI and TE were calculated correspondingly. Then, a new method was developed for simulating TC. All simulation results were validated by direct comparison to experimental measurements. Next, the polymer structure data available from the simulations was used to develop simple empirical models to predict VI, TE, and TC. Although these models require information from the simulation, they are far less computationally expensive and so can be used to predict performance metrics rapidly and with reasonable accuracy. Finally, the efficacy of the empirical models was evaluated for a sixth fluid that was not part of the model development.

2. Materials and Methods

2.1. Test Fluids

The five ISO VG32 fluids evaluated in this study are listed in Table 1. These fluids were formulated by blending five polymers with varying chemistries and degrees of branching with 3 mm²/s group III base oil such that the formulated fluids had a kinematic viscosity of 7 mm²/s at 100 °C. For this study, we chose five different branched and linear polymers with number average molar mass ranging from 3.0 to 8.5 kg/mol and viscosity ranging from 480 to 997 mm²/s. The names of the fluids start with FKV to indicate they had similar/fixed kinematic viscosity and end with the abbreviation of the polymer additive with which they were formulated.

FKV-PAO was formulated by blending 3 mm²/s group III base oil with 15.7 wt.% of polyalphaolefin (PAO) polymer having number average molar mass of 5.0 kg/mol, polydispersity index (PDI) of 1.1, density of 0.86 g/cc, and viscosity of 500 mm²/s. The PAO in the FKV-PAO fluid comprised 100 wt.% 1-decene monomer. The polyisobutylene (PIB) in FKV-PIB fluid had 100 wt.% isobutylene monomer. The butadiene isoprene (BDIP) polymer in FKV-BDIP fluid had 50 wt.% butadiene and 50 wt.% isoprene monomers. The polyalkyl methacrylate (PAMA) polymer in FKV-PAMA fluid had 22 wt.% C12-methacrylate, 30 wt.% C13-methacrylate, 30 wt.% C14-methacrylate, and 18 wt.% C15-methacrylate monomers of varying branching patterned of alkyl chains. The methacrylate butadiene (MABD) polymer in FKV-MABD fluid had 6.0 wt.% methyl methacrylate, 8.5 wt.% butyl methacrylate, 75.5 wt.% lauryl methacrylate, and 10 wt.% butadiene. The BDIP and MABD polymers were saturated by hydrogenation. It is notable that the PIB and the BDIP are linear whereas the remaining three polymers PAO, PAMA, and MABD have varying degrees of branching. All the fluids were formulated with 6.5 wt.% Anglamol 99 (32% S, 1.7% P, 0.05% N) antiwear and high-pressure additive package.

Table 1. Description of the test fluids and polymers. The colors scheme introduced here will be used to identify the fluids subsequently in this paper.

Properties	FKV-PAO	FKV-PIB	FKV-BDIP	FKV-PAMA	FKV-MABD
Base stock ID	GIII 3 mm²/s	GIII 3 mm²/s	GIII 3 mm²/s	GIII 3 mm²/s	GIII 3 mm²/s
Polymer ID	PAO	PIB	BDIP	PAMA	MABD
Monomer(s)	1-decene	isobutylene	butadiene, isoprene	C12-C15 methacrylate	methacrylate, butadiene
Polymer treat rate, wt.%	15.7	14.6	9.8	20.8	15.8
No. avg. molar mass of polymer, kg/mol	5.0	2.1	3.0	8.5	4.3
Polydispersity index of polymer	1.1	1.8	2.8	1.7	2.8
Density of polymer at 15.6 °C, g/cc	0.86	0.91	0.86	0.94	0.95

Viscosity of Polymer at 100 °C, mm²/s	500	2500	997	480	-

2.2. Rheological and Traction Measurements

Three different instruments (see Figure S1) were used to measure the Newtonian viscosities and TC of the fluids. The Newtonian viscosity was measured at 40 and 100 °C so that the VI and TE of the fluids could be characterized. First, a viscometer was used to measure the kinematic viscosity of all fluids. These measurements were conducted per the ASTM D-445 test standard [72]. Second, a Cannon StressTech HR Oscillatory Rheometer was used to measure the dynamic viscosity of all fluids, except for FKV-PAO and FKV-PIB. The shear rate was varied from 10 to 1000 1/s, with 15 measurements taken at logarithmically spaced intervals in that range. This procedure was repeated three times for each fluid to report the average Newtonian viscosity values at each temperature. The standard deviation of the average of the three measurements was around 0.2-0.3 mPa.s. Third, a PCS Instruments Mini-Traction Machine (MTM) was used to measure the traction coefficient of all fluids at 40 °C in the full film lubrication regime. The tests were performed at an entrainment speed of 1.0 m/s, load of 75 N, and slide-to-roll ratio of 20.0%. Both the ball and disk specimens were AISI 52100 steel with an elastic modulus of 207 GPa and Poisson's ratio of 0.3. The diameter of ball was 19.05 mm. The average roughness of ball and disk were 12.0 and 6.0 nm, respectively. The traction coefficient measurement of each fluid was performed once per fluid. The shear rate experienced by the fluid during these tests was estimated based on the experimental parameters and estimated film thickness, as described in the supplementary information Section S10, to be 1.6×10^6 1/s. All the experimental data are tabulated in Section S2 of the supplementary material. For some fluids, viscosity and traction coefficient were measured with and without the Anglamol 99 additive. The comparison of the properties of three fluids with and without 6.5 wt.% of Anglamol additive package is shown in Figures S2 and S3. It was found that the fluids formulated with the additive package had higher viscosity, thickening efficiency, and traction coefficient than the fluids formulated without the additive package. However, the comparison also shows that the fluids with and without additive exhibited consistent trends.

2.3. Molecular Dynamics Simulations

The model systems were created to reproduce the physical fluids studied experimentally (Table 1). The model structures of the base oil and polymer molecules are shown in Figure 1. The differences between the physical and model fluids were the PDI, the base oil chemistry, and the presence of the additive package. First, for the virtual formulations, a PDI of 1.0 was assumed whereas the PDI of the physical fluids was between 1.1 and 2.8. Generally in polymer melts, as the PDI increases, the Newtonian viscosity decreases and the shear thinning behavior becomes more pronounced [73]. However, in our case, this effect should be negligible due to the small concentration of the polymer and low viscosity of the solutions. Second, since the composition of group III (3 mm²/s) base oil was unknown, a model 3 mm²/s base oil was created from 25 wt.% PAO 2 mm²/s (PAO2) and 75 wt.% PAO 4 mm²/s (PAO4). Previous gas chromatography-mass spectroscopy measurements reported that PAO2 comprised nearly 100 wt.% dimer of 1-decene whereas PAO4 comprised 50 wt.% trimer of 1-decene + 50 wt.% tetramer of 1-decene [74]. More details, including viscosity measurements (Table S3) and a sample calculation of the ratios of each molecule (Table S4), about the formulation of the 3 mm²/s PAO base oil can be found in Section S3 of the supplementary material. Group III base oils usually have lower VI than group IV oils (i.e., PAO base oils) [75], so the model fluids may have higher VI than their viscosity counterparts. Lastly, the models did not contain the additive package. Therefore, these model fluids were created with 6.5 wt.% more 3 mm²/s group III base oil than the physical fluids. For example, the model FKV-PAO comprised 15.7 wt.% of PAO with 84.3 wt.% of 3 mm²/s group III base oil in the FKV-PAO fluid.

The model systems were created using Material Studio software. More details about each model system, including composition, simulation box size, and number of each type of molecule, are given in Table S5. For all simulations, a time step of 1.0 fs was used, and periodic boundary conditions were applied in all directions. An orthogonal simulation box ($30 \times 3 \times 3$ nm³) was used to allow the molecules to elongate in response to shear applied in the direction of the long side of the box in the traction simulations. This model design minimized finite-size effects [76] where molecules might unphysically interact with themselves across the periodic boundary. Not all properties are affected by the system size; for example, the shear viscosity showed no significant system-size dependences, unlike the diffusion coefficient [77]. Nevertheless, a large enough simulation box was used to reduce pressure and stress fluctuations [78], enabling accurate and reliable calculation of the mechanical properties of a polymer system [79].

All atomic interactions were described using a united atom (UA) potential. UA potentials are known to accurately describe the viscosity of hydrocarbons for broad range of temperatures, pressures, and shear stresses according to

numerous past studies [45,80–87]. The UA parameters were selected from Transferable Potentials for Phase Equilibria (TraPPE-UA) developed for branched alkanes, alkenes, alcohol, aldehyde, ketone, methacrylate, and carboxylic acids [88–99]. Details about the UA potential and force field parameters are given in Section S5. Simulations using the TraPPE-UA force field were performed with a spherical cutoff of 1.4 nm and analytic tail corrections for the Lennard–Jones interactions. The covalent bonds were modeled by a harmonic potential with the force constants [98,99]. Dynamic simulations were run using Large Atomic/Molecular Massively Parallel Simulation (LAMMPS) software [100].
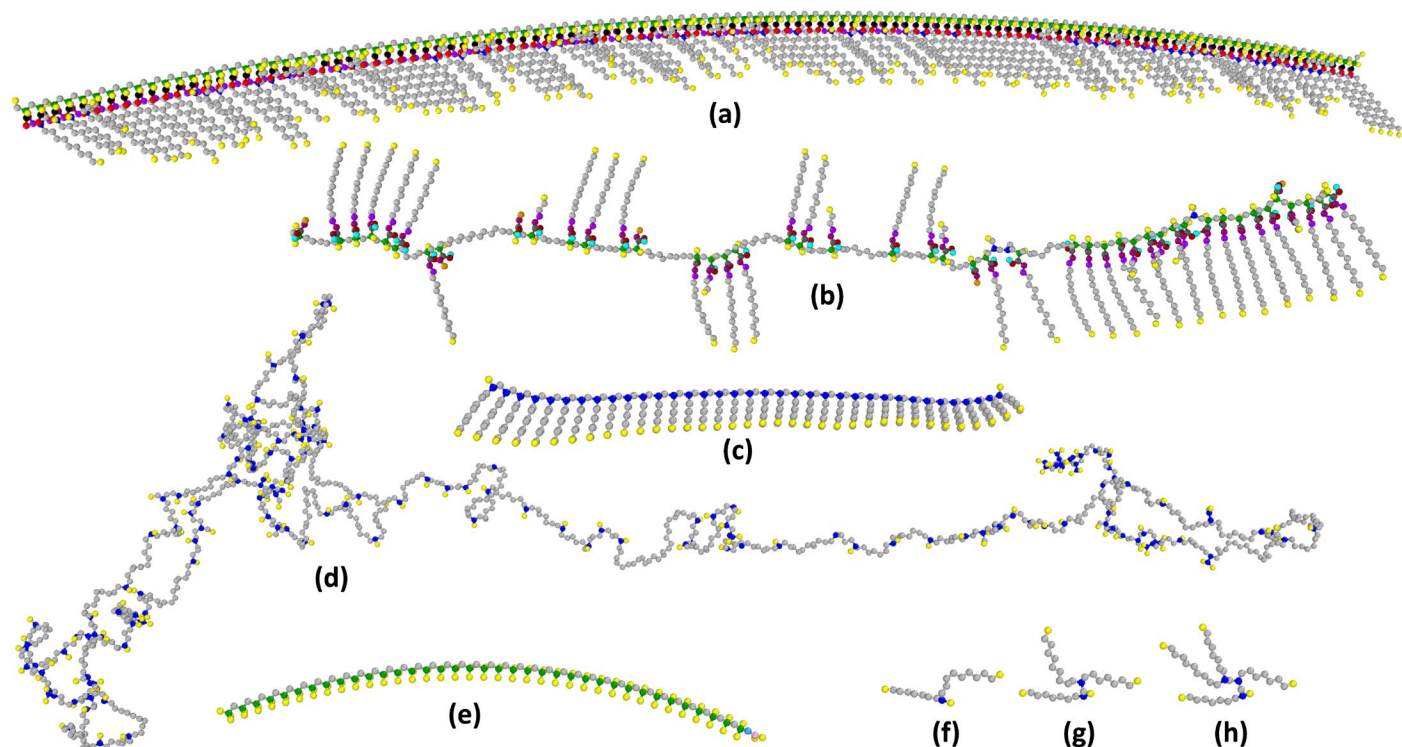

Figure 1. Structure of the molecules in united atom representation: (a) PAMA polymer, (b) MABD polymer (c) PAO polymer, (d) BDIP polymer, (e) PIB polymer, (f) dimer of 1-decene, (g) trimer of 1-decene, and (h) tetramer of 1-decene. The sphere colors represent the following pseudoatoms: yellow-CH_3, silver-CH_2, blue-CH, green-C, black-C(=O), red-O(=C), magenta-O, purple-CH_2(-O), orange-CH_2(-O), dark grey-CH(-OH), cyan-H(-O) sky blue-CH(=C), and pink-C(=CH).

To prepare the model system, an energy minimization of the system was performed using the conjugate gradient algorithm. The system density was then equilibrated at 1.0 atm and either 40 or 100 °C for 50 ns in the isothermal–isobaric (NPT) ensemble using the Nosé–Hoover thermostat and barostat [101,102], with damping coefficients of 100 and 125 fs, respectively. Then, while maintaining a constant temperature for 10 ns in the canonical (NVT) ensemble, the simulation box was deformed until the density of the fluid reached the average density computed from the last 10 ns of the previous NPT simulations. Finally, the system was equilibrated using the final configuration from NVT as the initial configuration for 5 ns in the microcanonical (NVE) ensemble. This way, the desired equilibration state of the system was achieved while avoiding interference with the dynamics of the system [103].

To calculate viscosity, following the equilibration process, further equilibrium molecular dynamics simulations were carried out. Specifically, we used the Green–Kubo approach, which relates the viscosity to the time integral of the stress autocorrelation function [103,104], as in Equation (1). Simulations were equilibrated again for 2 ns in the NPT ensemble followed by NVE ensemble production runs. The pressure tensor components were saved every 5 fs for 5 ns at 100 °C and 20 ns at 40 °C during the NVE simulation. An average low-shear viscosity $\langle\eta(t)\rangle$ and its standard deviation $\langle\sigma(t)\rangle$ values were calculated from 20 to 40 NVE trajectories and by applying the Green–Kubo formalism following the time decomposition approach [104] (see Figure S7). The standard deviation of viscosity was calculated from the multiple NVE trajectories using Equation (2). This approach has been used previously in many studies and has been found to provide accurate and reliable viscosity.

$$\eta(t) = \frac{V}{6k_B T} \int_0^\infty \langle P_{\alpha\beta}(t) \cdot P_{\alpha\beta}(0) \rangle dt \qquad (1)$$

$$\text{Standard deviation,} \langle \sigma(t) \rangle = \left\langle \sqrt{\frac{1}{n-1} \sum_{i=1}^{n} (\eta(t)_i - \langle \eta(t) \rangle)^2} \right\rangle \qquad (2)$$

In the Green-Kubo formalism, η is the dynamic viscosity, V is the volume of simulation box, T is the temperature, k_B is the Boltzmann constant, $P_{\alpha\beta}$ is the stress tensor, t is the time, $\langle \eta(t) \rangle$ is the average dynamic viscosity, $\langle \sigma(t) \rangle$ is the standard deviation, and n is the number of NVE trajectories. All six components of stress tensor $P_{\alpha\beta}$ were used to calculate viscosity and used in the denominator of Equation (1). Figure 2 shows representative results from viscosity simulations of FKV-PAO fluid at 40 °C. In this figure, black and red curves represent the average viscosity and standard deviation, respectively, calculated from 20 NVE trajectories which are shown by 20 blue curves. Each blue curve in Figure 2 is made up of 40 blue square symbols which correspond to the viscosity calculated by taking the time integral of stress tensors every 0.5 ns simulation time, as described by Equation (1). The trajectories, with their average viscosity and standard deviation curves for all fluids and two temperatures are provided in Figure S7. An average kinematic viscosity $\langle \nu(t) \rangle$ value from multiple NVE trajectories was calculated by $\langle \eta(t) \times \rho \rangle$. Here, ρ is the density of a fluid calculated from the last 10 ns of NPT ensemble while equilibrating model systems. To simulate accurate viscosity, simulation parameters such as system size, damping and drag coefficients for thermostat and barostat were optimized for the forcefield parameters (see Figure S5). In addition, the dependence of viscosity on simulation parameters such correlation length, simulation time, and number of NVE trajectory was also studied (see Figure S6). This vital analysis suggested that the accuracy of viscosity simulations is most highly dependent on correlation length followed by simulation time and that using multiple NVE trajectories is only important to produce reliable viscosity. This approach was used to calculate the Newtonian viscosity of fluids at 40 and 100 °C. These temperatures were chosen to enable calculation of viscosity index as per the ASTM D2270 standard [6] and to reflect the temperature range experienced by lubricants used as hydraulic and automobile fluids.
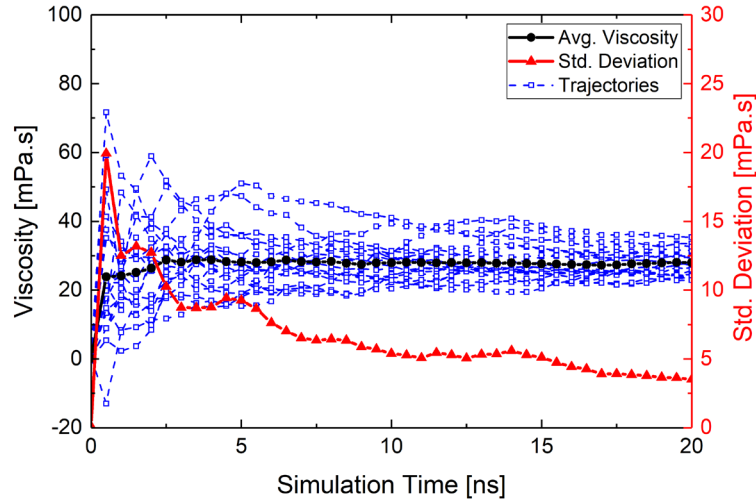

Figure 2. Representative viscosity calculation for FKV-PAO fluid at 40°C using the time decomposition approach from 20 NVE trajectories. The blue symbols represent the viscosity obtained from Equation (1) by integrating the stress autocorrelation at a given simulation time. The average viscosity and standard deviation are shown by black and red curves, respectively.

To calculate traction coefficient (TC) at different shear rates, loading simulations and then non-equilibration molecular dynamics (NEMD) simulations were carried out. The most common approach to simulating TC is to model the dynamic behavior of fluid molecules confined between two solid surfaces [67,68,70,71,105,106]. In this methodology, solid surfaces are slid with a constant velocity to shear the lubricant, while a constant pressure is applied in the surface-normal direction [67,68,70,71,105,106]. The explicit modelling of the solid surfaces results in a large number of atoms in the simulation which presents a challenge in the case of fluids formulated with large polymer molecules, as in this study. Further, the typical approach requires accurate modeling of solid-liquid interactions, which can be problematic for real

engineering materials. Therefore, we developed a simple approach where the pressure and shear are applied directly to the fluid molecules by deforming the simulation box. This approach is appropriate for modeling the physical experiment that was performed in the full film lubrication regime in which traction is due to resistance to shear within the fluid, as opposed to interactions between confining walls. However, a limitation of this approach is that it is not suitable for investigating the effect of interface chemistry.

In the first step of the traction simulations, simulations were carried out to apply a pressure of 0.5, 1.0, or 1.5 GPa. For this, the size of the simulation box was decreased in the z-direction until that the component of stress tensor, or pressure, in the z-direction P_{zz} reached the target value. This approach is equivalent to performing simulations in the NPT ensemble to achieve a target value of P_{zz}. Then, the simulation with the new size was run in the NVT ensemble at 40 °C for 5 ns followed by the NVE ensemble for 5 ns to relax the system. In the second step, NEMD simulations were carried out at five shear rates, $\dot{\gamma}$, 1×10^7, 1×10^8, 1×10^9, 1×10^{10}, and 1×10^{11} 1/s. In NEMD simulations, the shear rate was imposed on the simulation box by deforming it in the x-direction for 20-300 ns, depending on the shear rate. At the same time, the fluids were thermostatted using a Nosé Hover thermostat [101] and the SLLOD [107,108] equations of motion. Depending on the shear rate, 5–200 ns of time was allowed for the system to achieve steady-state before the normal pressure P_{zz}, shear stress P_{xz}, and velocities of the atoms in the direction of shear u_x were collected for post processing. It was determined that an NEMD simulation reached steady state if the goodness of a linear fit to the average atom velocities was 98% or greater. The average shear rate ($\dot{\gamma} = \partial u_x / \partial z$) was then calculated from the slope of the linear fit to the average atom velocities in the direction of shear u_x and divided by the simulation box length in z-direction L_z.
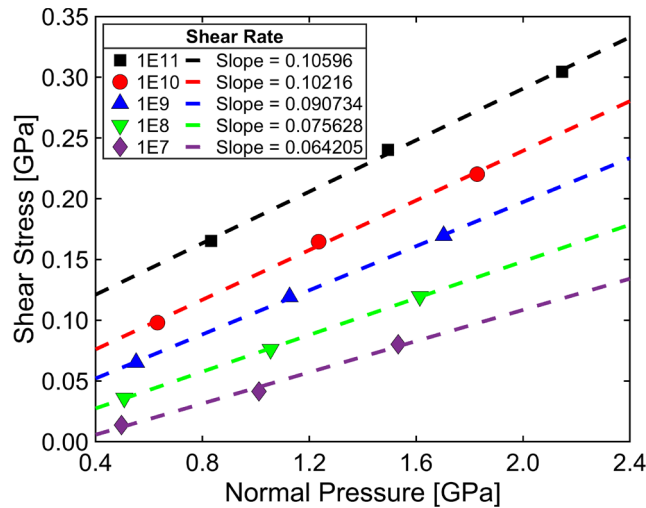

Figure 3. Shear stress vs. normal pressure from simulations of FKV-PAO at five different shear rates. The solid black, red, blue, and green symbols represent the simulation data at shear rates of 1×10^7, 1×10^8, 1×10^9, 1×10^{10}, and 1×10^{11} 1/s, respectively, whereas the dashed lines represent the linear fits. The slope of the linear fit at each shear rate is the TC, reported in the legend.

The traction simulations were conducted for each fluid at 40 °C and shear rates of 1×10^7, 1×10^8, 1×10^9, 1×10^{10}, and 1×10^{11} 1/s for each desired normal pressure of 0.5, 1.0, and 1.5 GPa. The average shear stress P_{xz} vs. normal pressure P_{zz} data was fit linearly at each shear rate, and the slope taken as the traction coefficient, as shown in Figure 3. The lowest shear rate achievable in the simulations was 1×10^7 1/s. However, the MTM measurements were performed with shear rates of approximately 1.6×10^6 1/s. To extrapolate the simulation data to this shear rate, we used the relationships between shear stress and shear rate and between normal pressure and shear rate. These relationships are expected to be follow a power-law where the exponent is much larger for normal stress than shear stress [109]. The shear stress and normal pressure were fitted to $P = a + b\dot{\gamma}^c$, where a, b, and c are fitting parameters, as shown in Figure 4. The R-squared values of the fits were greater than 99.5% for all the cases. Then, those fitting parameters were used to predict the shear stress and normal pressure at lower shear rates and then the traction coefficients at those shear rates are calculated, as shown in Figure 5. This traction simulation approach is very computationally efficient since it does not require using two solid surfaces nor any assumptions about solid-fluid interactions. Linear fits of the shear stress vs. normal pressure for all fluids with their extrapolated traction curves can be found in Figure S8.
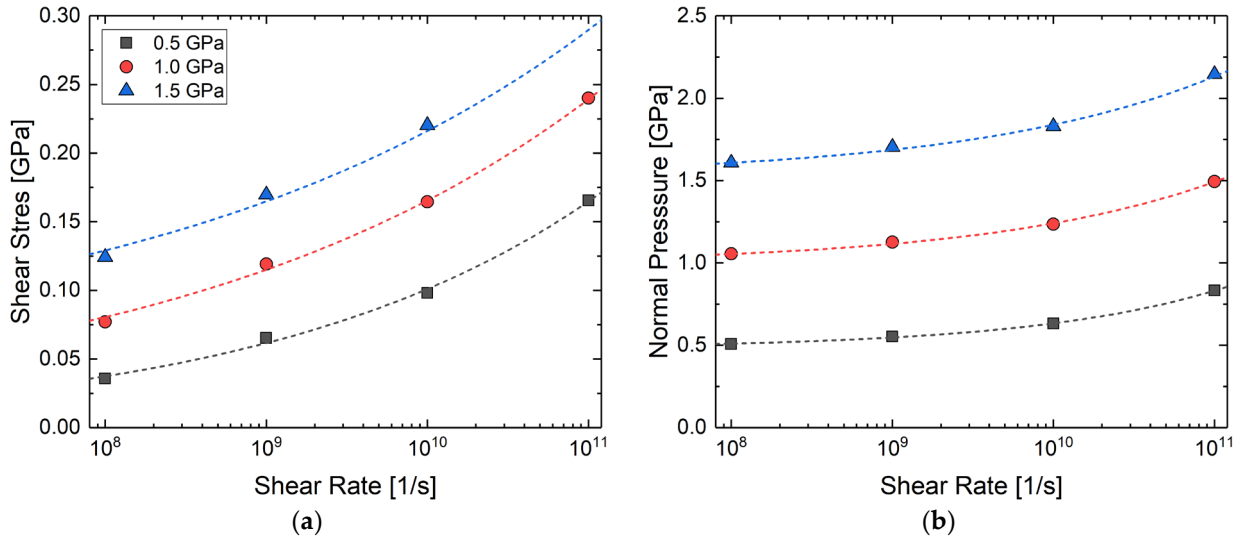
Figure 4. Simulation-calculated (a) shear stress and (b) pressure as a function of shear rate for FKV-PAO at target pressures of 0.5, 1.0, and 1.5 GPa, shown as solid black, red, and blue symbols, respectively. The dashed lines represent power law fits.
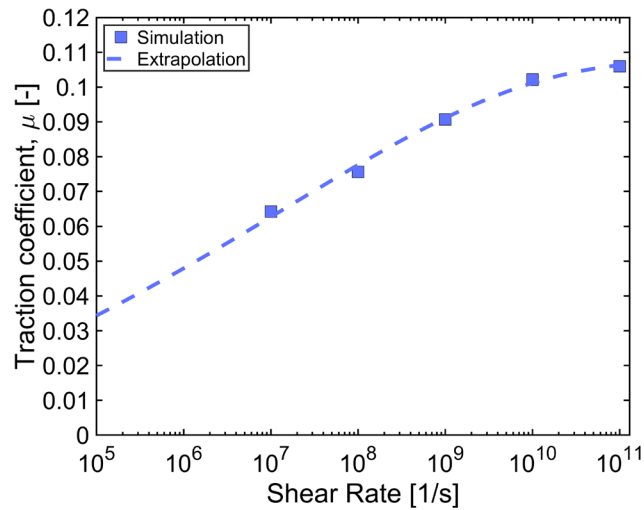

Figure 5. Extrapolated traction curve for FKV-PAO generated from the power law fit of shear stress and pressure. The blue dashed line represents the extrapolated curve whereas the solid blue squares represent the traction coefficients directly calculated from the simulation by the slope of linear fit of shear stress to normal pressure at those shear rates.

3. Results and Discussion

3.1. Validation of Simulation Approach

Figure 6 shows the kinematic viscosity measured experimentally and calculated using simulations for all fluids, including the base oil, at 40 and 100°C. The patterned bars are the measured viscosity whereas the solid bars are simulated viscosity at each temperature. The error bars are the standard deviation from multiple experimental measurements or simulation trajectories. Note that the standard deviation for the simulations is higher at 40 °C than at 100 °C because the stress autocorrelation takes greater amount of time to decay at lower temperature due to slower relaxation dynamics, requiring longer simulation durations [110,111]. The effect of simulation duration on viscosity error at different temperatures is illustrated in Figure S6. Regardless, the simulation results agree with measured values within the reported error.
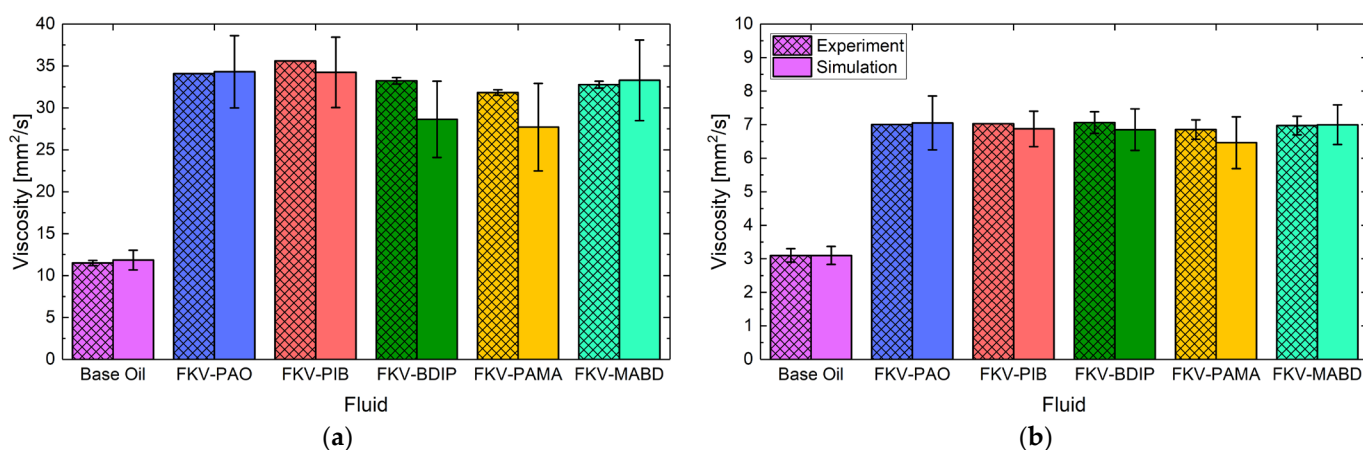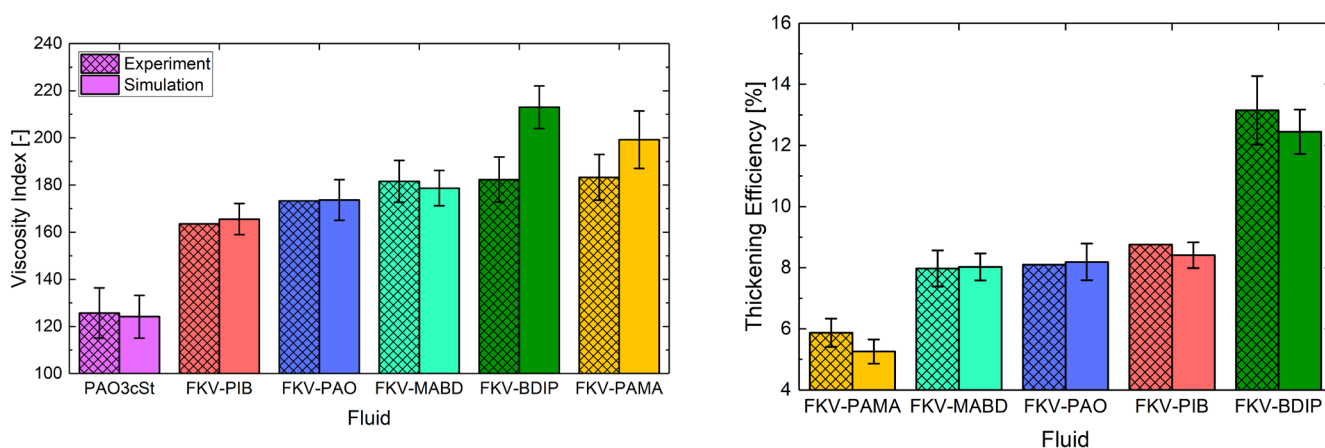

Figure 6. Experimentally measured (patterned bars) and simulation calculated (solid bars) kinematic viscosity of the fluids at (a) 40 and (b) 100°C. The error bars represent the standard deviation calculated from multiple experiments and from multiple NVE trajectories (Equation (2)) in simulation.

The VI, shown in Figure 7(a), was calculated using kinematic viscosity at 40 °C and 100 °C per the ASTM D2270 [6] standard. This standard states that precision limits cannot be assigned to a calculated VI value. However, we have reported the uncertainty in VI propagated from the standard error of the mean viscosity, as a guide for evaluating the statistical significance of differences between fluids. The order of the mean fluid VIs calculated from experimental data is: Base Oil < FKV-PIB < FKV-PAO < FKV-MABD < FKV-BDIP < FKV-PAMA. The simulation trend of the mean VIs is: Base Oil < FKV-PIB < FKV-PAO < FKV-MABD < FKV-PAMA < FKV-BDIP, the same as in experiments except for the PAMA/BDIP fluids. The simulated VI is higher for FKV-BDIP and FKV-PAMA than measured experimentally. This difference is due to the underprediction of the viscosity of these fluids at 40 °C which can be attributed to the fact that the stress autocorrelation takes longer to decay for larger and more branched molecules due to slower relaxation dynamics, requiring longer simulation durations [110,111]. The average percent difference between experiment and simulation VI for all fluids is 4.98%. However, considering the sensitivity of VI on viscosity of the fluids this is still impressive prediction of VI by MD simulations.

Figure 7. (a) Viscosity index of the fluids calculated using the measured (patterned bars) and simulated (solid bars) kinematic viscosities at 40 and 100 °C. (b) Thickening efficiency of the fluids calculated using the experimentally measured (patterned bars) and simulation-calculated (solid bars) kinematic viscosities at 100 °C. The error bars represent the viscosity error propagated using the VI and TE equations. The error bars represent uncertainty in VI and TE propagated from the standard error of the mean of the viscosities.

The TE at 100 °C was calculated from the measured and simulated kinematic viscosity [7]. Since the fluids had different concentrations of polymer, the thickening efficiencies were normalized by the polymer concentration to enable direct comparison of the fluids, as described by Equation (3).

$$\text{TE} = \frac{v_{0s} - v_{0B}}{v_{0B}} \frac{1}{C} \times 100 \tag{3}$$

Here, C is the concentration of polymer, v_{0s} is the Newtonian viscosity of the polymer-containing fluid, and v_{0B} is the Newtonian viscosity of base oil. The results are shown in Figure 7(b). The TE of base oil is not included in these figures since it is the reference and therefore has a TE of zero. In this figure, the patterned bars represent TE calculated using measured kinematic viscosity and the solid bars represent TE calculated using simulated kinematic viscosity. Note that the simulation TE reflects the increase in viscosity due to just the polymer whereas the experimental TE indicates viscosity increase due to both polymer and Anglamol additive package. However, the effect of the additive package on TE is small and the trends are consistent with and without additive, as shown in Figure S2b. The order of the mean TE in Figure 7(b), calculated from either simulation or experimental data, is: FKV-PAMA < FKV-MABD < FKV-PAO < FKV-PIB < FKV-BDIP.

It can be concluded from these comparisons that the properties derived from simulation-calculated viscosity, such as VI and TE, are in good agreement with experimental values. Further, comparing the trends in Figures 7(a) and 7(b) reveals that a polymer that has higher VI might not also have high TE. Subsequently, we will refer to the mean values of VIs and TEs.
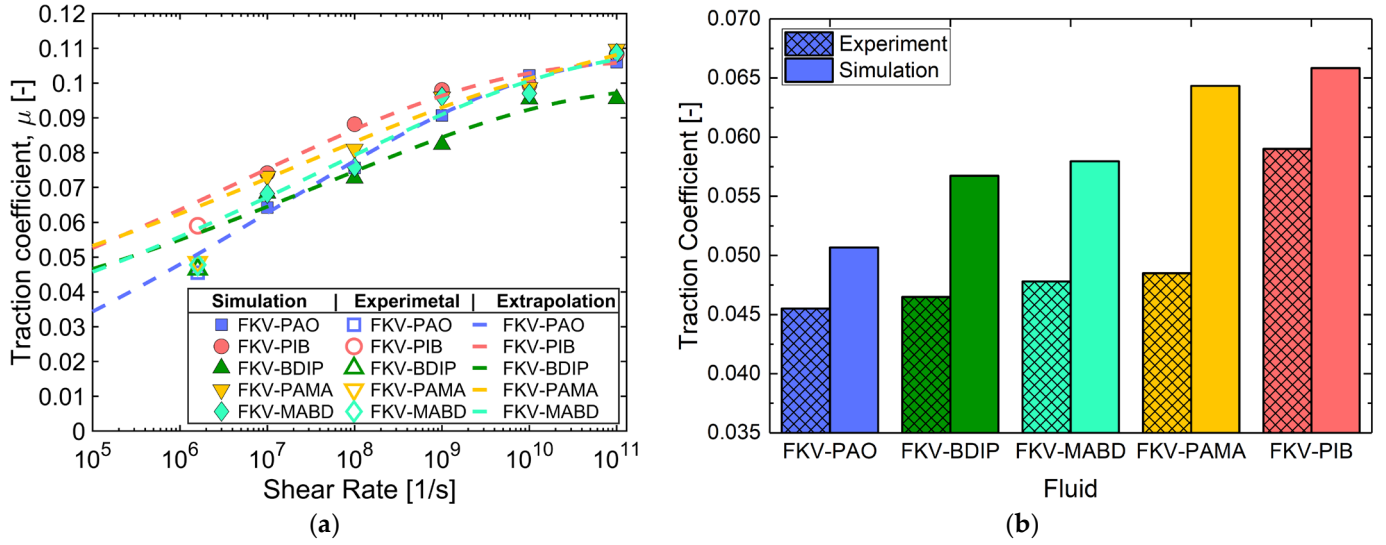
Figure 8. (a) Traction coefficient at 40 °C as a function of shear rate. Here, the solid symbols represent the traction coefficients calculated directly from simulations, the hollow symbols represent the measured traction coefficients, and the dashed lines represent the extrapolated traction curve from simulations. (b) Comparison of measured traction coefficient (patterned bars) and the extrapolated simulation traction coefficient (solid bars) at 40 °C and a shear rate of 1.6×10^6 1/s.

Figure 8(a) shows the traction coefficient results as a function of shear rate where the hollow symbols are data from experiments and solid symbols are data from simulations. Since the simulations could not directly model the shear rate in the experiments, due to the timescale limitation of the simulation method, we extrapolated the high shear rate traction coefficients from simulations (solid symbols in Figure 8a) to the experimental shear rate of 1.6×10^6 1/s. The extrapolation procedure is described in the Materials and Methods section. The dashed lines in Figure 8(a) are the extrapolated traction curves. The experimental data and values obtained from extrapolation of simulation results are shown in Figure 8(b). The experimental data in Figure 8b is the same as the hollow symbols in Figure 8a. The overprediction of TC by MD simulations could be due to the fact that TC decreases with increasing film thickness [112] and the simulated film thickness is much smaller than that in experiments. Although the simulations overpredict TC for most fluids, the trend from both experiments and simulations is the same: FKV-PAO < FKV-BDIP < FKV-MABD < FKV-PAMA < FKV-PIB. This good agreement demonstrates that the simulation and extrapolation approaches developed here are useful for modeling the traction coefficient of real lubricants in the full film lubrication regime. Note that the experimental TC includes the effect of the Anglamol additive package while the simulation TC does not. However, as reported in Table S2 and Figure S3b, while the additive increases TC, the trends between fluids are the same with and without the additive.

3.2. Effect of Structure on Viscosity Index, Thickening Efficiency, and Traction Coefficient

To understand the trends in VI and TE, we related these parameters to the molecular and structural properties of polymers. The two properties to which VI and TE have been correlated are the percent of the molecular weight of the polymer in the backbone (M_{wp}) and the radius of gyration (R_g) of the polymer [2,21,47,48,55,113].

First, it has been proposed that VI is correlated to radius of gyration [2,47,113]. Polymers of higher molecular weight and narrower molecular weight distribution usually have larger VI [33]. A recent experimental study [113] reported that the rate of increase in radius of gyration with temperature was faster for a linear (high M_{wp}) than branched (low M_{wp}) PAMA polymers and that the linear PAMA had higher VI [113]. As shown in Figure 9, VI appears to be weakly correlated with M_{wp} and moderately correlated with R_g. However, VI does not vary monotonically for the five fluids studied here with either parameter, indicating that neither parameter can capture the trend on its own. Figure 9 shows that, when two polymers have similar M_{wp}, the fluid with the polymer having larger R_g has higher VI. Also, generally, fluids with polymers having larger R_g have higher VI. But, if two polymers have similar R_g, then the fluid with smaller M_{wp} has higher VI. These results suggest that both parameters must be considered to understand the VI trends.
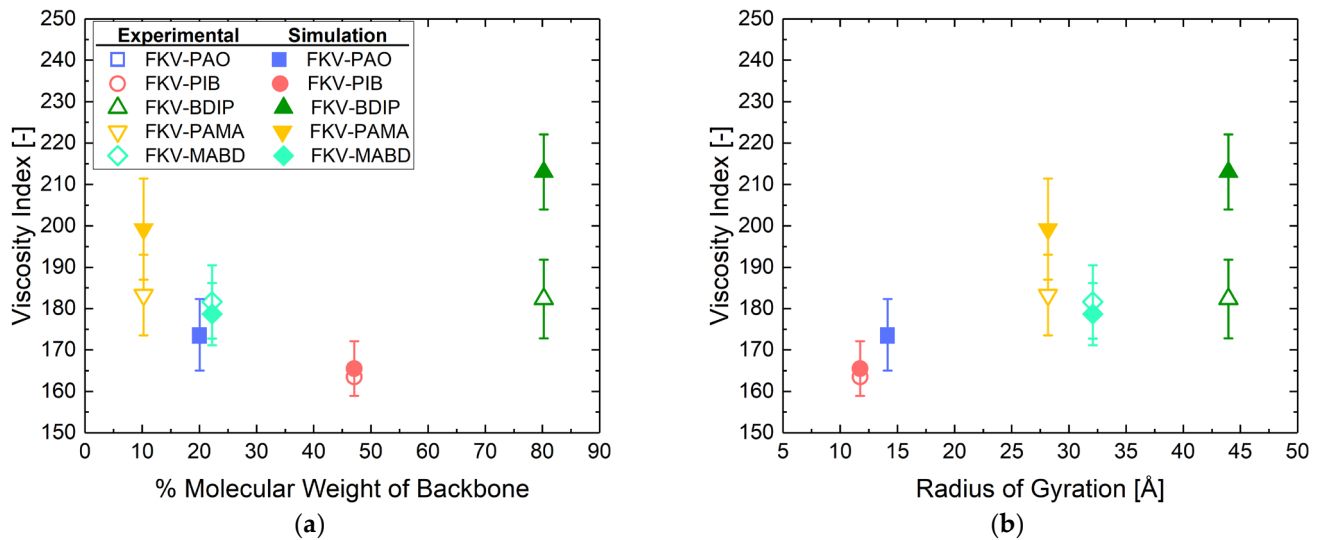
Figure 9. Viscosity index of the fluids as a function of (**a**) percent of the polymer molecular weight in the backbone, and (**b**) simulation-calculated radius of gyration. The hollow symbols represent viscosity index calculated using measured kinematic viscosity whereas the solid symbols represent viscosity index calculated using simulated kinematic viscosity. The error bars represent uncertainty in VI propagated using the standard error of the mean of the viscosity.

It has been suggested that TE increases with percent of the molecular weight of the polymer in the backbone (M_{wp}) [21,33,34]. One study [21] reported a linear increasing trend of TE with M_{wp} for OCP, PIB, and PAMA polymers. A similar trend of decreasing TE with increased branching (that is lower M_{wp}) in polyethylene polymers was observed in a study of high shear stability VI improvers [33]. For the fluids studied here, Figure 10 shows that TE generally increases with M_{wp}, except for the FKV-MABD fluid. This indicates that the linear polymers with higher M_{wp} have a greater thickening effect. However, the increase in TE with M_{wp} is nonmonotonic, and TE both increases and decreases with R_g. Between the FKV-PIB, FKV-PAO, and FKV-PAMA fluids, TE decreases as R_g increases, but the opposite trend is observed for FKV-MABD and FKV-BDIP fluid. Thus, the dependence of TE is different than that exhibited by VI: VI generally increases with R_g but varies nonmonotonically correlated with M_{wp}, whereas TE generally increases with M_{wp} but varies nonmonotonically with R_g. Importantly, neither of these two properties cannot individually capture the trends of VI and TE.
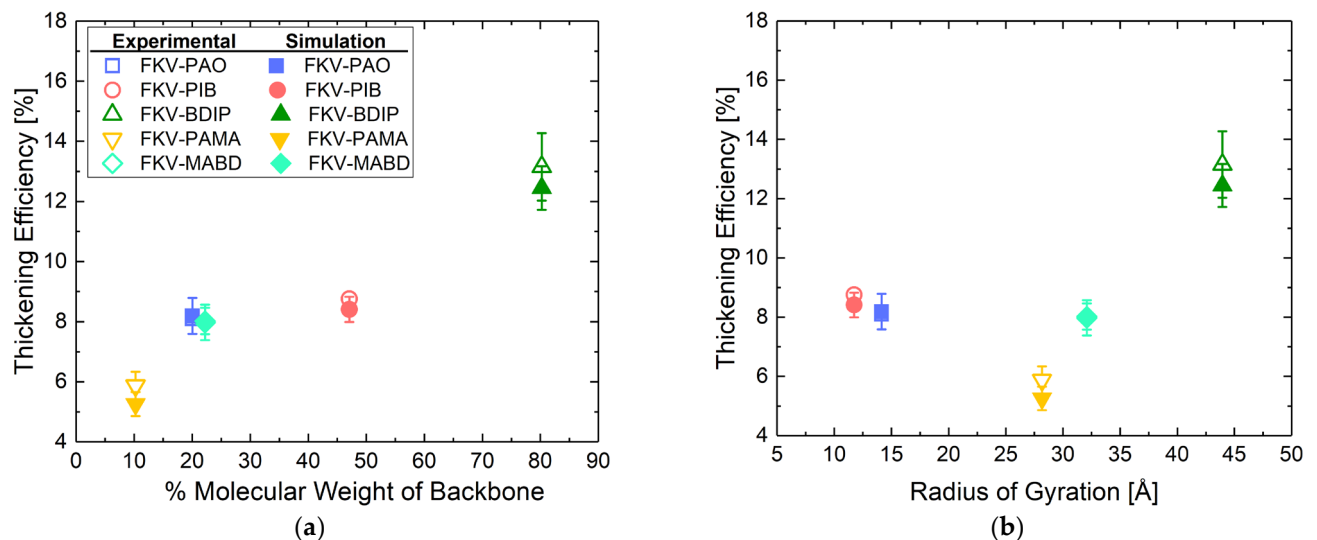

Figure 10. Thickening efficiency of the fluids at 100 °C as a function of (**a**) percent of the polymer molecular weight in the backbone, and (**b**) simulation-calculated radius of gyration. The hollow symbols represent thickening efficiency calculated using measured kinematic viscosity whereas the solid symbols represent thickening efficiency calculated using simulated kinematic viscosity. The error bars represent uncertainty in TE propagated using the standard error of the mean of the viscosity.

The results in Figure 8(b) show that fluids formulated with linear polymers (OCP and BDIP) have lower TC than the fluids formulated with branched polymers (MABD, PAMA, and PAO). A similar trend was previously reported

[67] where a higher TC of cyclohexane compared to the benzene was explained by the interlocking of cyclohexane molecules due to their chair conformation as opposed to the plane-shape of the benzene molecules. However, no prior study investigated the effect of polymer structure on the TC. So, to be consistent with the analyses performed for VI and TE, TC was analyzed as a function of M_{wp} and R_g, as shown in Figure 11. Generally, the TC decreases with increasing M_{wp} and R_g of the polymer. However, like VI and TE, the trend is not monotonic. This means that there are likely to be other parameters that correlate to the performance of these lubricants. Therefore, we next evaluated other molecular properties and their potential correlation to VI, TE, and TC.
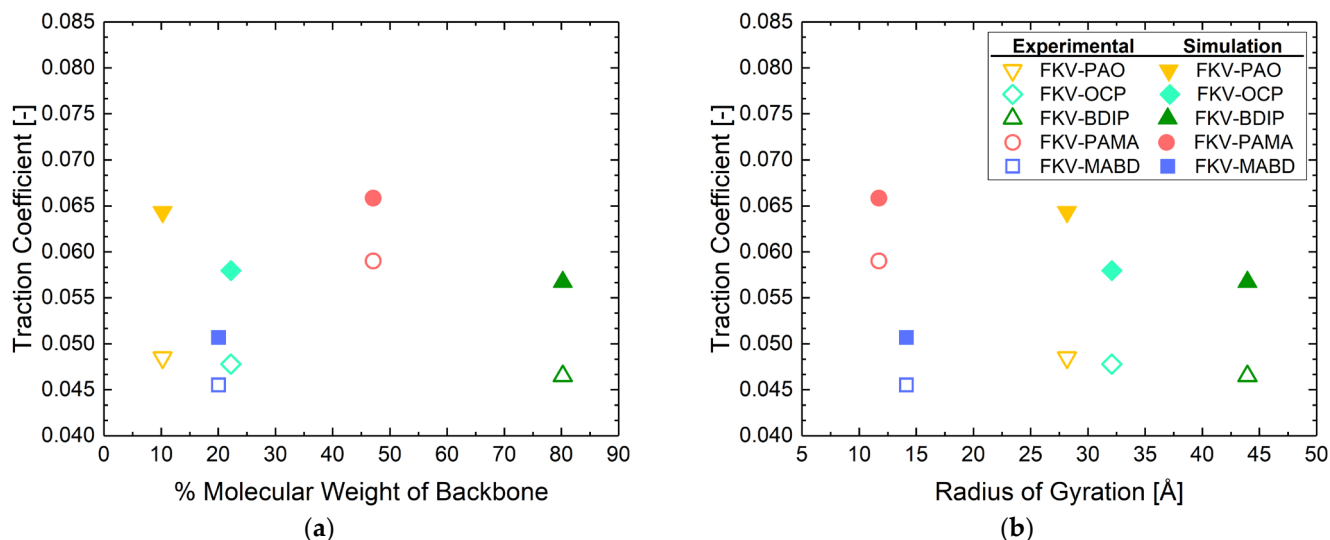

Figure 11. Traction coefficient of the fluids at 40 °C and MTM test conditions as a function of (**a**) percent of the polymer molecular weight in the backbone, and (**b**) simulation-calculated radius of gyration. The hollow symbols represent TC measured using a MTM machine whereas the solid symbols represent the TC calculated at MTM conditions by extrapolating the traction curve from simulations at high shear rates.

3.3. Predictive Models for Viscosity Index, Thickening Efficiency, and Traction Coefficient

To understand the differences between the fluids studied here, we calculated 22 different properties of the polymers. Five of these properties were molecular weights known based on the chemistry of the polymers. These properties are the mass average molar mass (M_w), number average molar mass (M_n), total molecular weight (M_{wt}), percentage molecular weight in backbone (M_{wp}), and molecular weight in backbone (M_{wb}). In addition, we calculated 17 properties based on positions of atoms in the simulations. The simulation-calculated properties are molecules lengths (L_x, L_y, L_z), end-to-end distance (R), radius of gyration (R_g), elements of gyration tensor ($R_{g,xx}^2$, $R_{g,yy}^2$, $R_{g,zz}^2$, $R_{g,xy}^2$, $R_{g,xz}^2$, $R_{g,yz}^2$), eigen values of gyration tensor (λ_x, λ_y, λ_z), and shape parameters (c, b, k). The three computed shape parameters are the asphericity b, the acylindricity c, and the relative shape anisotropy k [114,115]. The subscripts x, y, z refer to the coordinate axes of the simulation box. More details about each parameter are provided in Section S10.

We used best subset linear regression to identify models that correlate TE, VI, and TC with individual properties or combinations of the properties. First, the analysis was performed with just the five properties that are functions only of the polymer chemistry (M_w, M_n, M_{wt}, M_{wp}, and M_{wb}). Then, the analysis was repeated with all 22 properties, including both properties that are functions of only chemistry and those calculated in the simulations (L_x, L_y, L_z, R, R_g, $R_{g,xx}^2$, $R_{g,yy}^2$, $R_{g,zz}^2$, $R_{g,xy}^2$, $R_{g,xz}^2$, $R_{g,yz}^2$, λ_x, λ_y, λ_z, c, b, and k). The best models were selected out of more than 2 million possible combinations of these properties based on the R-squared value, standard error, and variance inflation factor (VIF) of the fit. Note that an ideal model would have an R-squared value of 1, a VIF of 1.0 and std. error of 0.0. Some models included only properties that are known based on the chemistry of the polymer whereas others included the best combination of properties out of all 22 properties. All structural parameters used in development of the VI and TE models are reported in Table S10.

The two best models for VI are given in Equations 4 and 5. Model A is a 2-term model based only on the first five properties, and Model B is a 3-term model based on all 22 properties. Model A is a function of molecular weight of

backbone and percentage of molecular weight in backbone ($M_{wp} = M_{wb}/M_{wt} \times 100$) of the polymer. Model B is a function of number avg. molar mass, molecule length, and relative anisotropy ratio of the polymer molecules. Since VI is calculated using the kinematic viscosities at 40 and 100 °C, the polymer properties were averaged over the two temperatures. The fit parameters have base units of kilogram as the unit of mass and angstrom as the unit of distance. The coefficients and values of the model selection criteria are given in Table 3. The coefficient of determination (R-squared) and VIF were higher, and the standard error (std. error) lower with Model B, indicating the model with the simulation parameter is a better predictor of VI. The magnitude of the coefficients indicates the degree to which each parameter is correlated to VI and the sign of the coefficient indicates and whether the correlation is positive or negative. For instance, in Model A, the coefficient for M_{wb} is 2.630 and for M_{wp} is -0.398. This means, M_{wb} is positively correlated whereas M_{wp} is negatively correlated (that is, if M_{wb} increases, VI will increase and if M_{wp} increases, VI will decrease) but M_{wb} is approximately 7 times more correlated to VI than M_{wp}. The coefficients of Model B can be interpreted similarly.

$$\text{A: VI} = a_0 + a_1 M_{wb} + a_2 M_{wp} \tag{4}$$

$$\text{B: VI} = a_0 + a_1 M_n + a_2 L_y + a_3 k \tag{5}$$

The two best models for TE at 100 °C are given in Equations 6 and 7. Model A, which was developed from only the first set of parameters, described TE as a function of total molecular weight of polymer and molecular weight of backbone of the polymer. When both sets of parameters were used, Model B was obtained which includes total molecular weight, end-to-end distance, and acylindricity of the polymer molecules. The polymer properties in Model B are from only the viscosity simulations at 100°C since the model was developed to predict TE at 100 °C. The coefficients and values of the selection criteria of these models are given in Table 2. The coefficients of TE models indicate that TE is negatively correlated to total molecular weight of the polymer. However, TE is positively correlated to molecular weight of backbone of the polymer like VI. This commonality in models of VI and TE suggest that a polymer could be designed to provide fluid with improved VI as well as improved TE (that, is an amount of polymer required to achieve a desired viscosity), as it the case, for the BDIP polymer which provided the highest TE and the second highest VI amongst the all polymer. From the developed VI and TE models, it can be said that both are highly dependent on the molecular weight because the viscosity of lubricants is highly dependent of the molecular weight [116].

$$\text{A: \%TE} = a_0 + a_1 M_{wt} + a_2 M_{wb} \tag{6}$$

$$\text{B: \%TE} = a_0 + a_1 M_{wt} + a_2 R + a_3 c \tag{7}$$

The three best models for TC are given in Equations 8, 9, and 10. There was no model based on only the first set of parameters which could give an R-squared value above 5%, so a two-term based model on both sets of parameters was developed and presented as Model A. Model A described TC as a function of molecular weight of the backbone and relative anisotropy ratio of polymer. When both sets of parameters were used to develop a three-term model, Model B was obtained, which includes mass average molar mass, percentage of molecular weight in backbone, and relative anisotropy ratio of the polymer. Neither of these models was sufficiently accurate, so Model C was identified which is a five-term model that has terms from both the sets of parameters. The terms in Model C include total molecular weight, percentage molecular weight in backbone, molecules length in the z-direction L_z, square of radius of gyration in zz-direction $R_{g,zz}^2$, and again the relative anisotropy ratio k of the polymers. These TC models were developed using both experimental and simulated TC. For the simulation data, the polymer properties at each shear rate were averaged over the three pressures simulated. The coefficients and values of the selection criteria of these models are given in Table 2. Note that the R-squared value is considerably lower for the TC than for the VI and TE models due to the fact that TC data from a wide range of shear rates (1.6×10^6 - 1×10^{11} 1/s) was used in the fitting. As shown in Figure 10(a), TC increases nonlinearly with shear rate whereas all the empirical models to which the data is fit are linear.

The coefficients for Model C in Table 2 show that the percentage of molecular weight in the backbone of the polymer M_{wp} and polymer length in the direction of normal pressure L_z are negatively correlated whereas total molecular weight of polymer M_{wt}, square of radius of gyration in zz-direction $R_{g,zz}^2$ and relative anisotropy ratio k are positively correlated to TC. Of the five terms in Model C, the relative anisotropy ratio k is the most correlated and the square of

the radius of gyration in the zz-direction $R^2_{g,zz}$ is the least correlated to TC. The signs of these coefficients also make physical sense. For instance, the TC of each fluid increases with shear rate whereas L_z decreases and k increases with shear rate (see Table S11), so the sign of coefficient of L_z is negative and of k is positive. All structural parameters used in the development of the TC models are listed in Table S11.

$$A: TC = a_0 + a_1 M_{wb} + a_2 k \tag{8}$$

$$B: TC = a_0 + a_1 M_w + a_2 M_{wp} + a_3 k \tag{9}$$

$$C: TC = a_0 + a_1 M_{wt} + a_2 M_{wp} + a_3 L_z + a_4 R^2_{g,zz} + a_5 k \tag{10}$$

Table 2. Coefficients and selection criteria for predictive models of VI, TE, and TC. Kilogram as the unit of mass and angstrom as the unit of distance were considered for these parameters.

Model		A	B	C
VI	Coefficients	$a_0 = 180.143$ $a_1 = 2.630$ $a_2 = -0.398$	$a_0 = 158.841$ $a_1 = 0.341$ $a_2 = 0.573$ $a_3 = -29.264$	No Need
	Selection Criteria	$R^2 = 0.932$ $VIF = 2.688$ $std.\ Error = 3.123$	$R^2 = 1.000$ $VIF = 7.119$ $std.\ Error = 0.004$	No Need
TE	Coefficients	$a_0 = 8.300$ $a_1 = -0.131$ $a_2 = 0.534$	$a_0 = 11.099$ $a_1 = -0.078$ $a_2 = -0.108$ $a_3 = 0.008$	No Need
	Selection Criteria	$R^2 = 0.997$ $VIF = 1.106$ $std.\ Error = 0.204$	$R^2 = 1.000$ $VIF = 2.510$ $std.\ Error = 0.018$	No Need
TC	Coefficients	$a_0 = 2.46 \times 10^{-2}$ $a_1 = -42.87 \times 10^{-4}$ $a_2 = 11.40 \times 10^{-2}$	$a_0 = 5.68 \times 10^{-2}$ $a_1 = -36.14 \times 10^{-4}$ $a_2 = -10.73 \times 10^{-4}$ $a_3 = 17.35 \times 10^{-2}$	$a_0 = 10.70 \times 10^{-2}$ $a_1 = 8.02 \times 10^{-4}$ $a_2 = -5.43 \times 10^{-4}$ $a_3 = -23.47 \times 10^{-4}$ $a_4 = 1.80 \times 10^{-4}$ $a_5 = 6.29 \times 10^{-4}$
	Selection Criteria	$R^2 = 0.629$ $VIF = 2.181$ $std.\ Error = 0.013$	$R^2 = 0.746$ $VIF = 3.396$ $std.\ Error = 0.011$	$R^2 = 0.824$ $VIF = 18.756$ $std.\ Error = 0.009$

3.4. Predictive Model Validation

To validate the predictive models, a new fluid was physically formulated. The new fluid, called F-ROMP, comprised a 5.8 wt.% new polymer ROMP ($C_{704}H_{1410}$), shown in Figure 12, with 48.1 wt.% Nexbase 3030 base oil and 39.6 wt.%

Nexbase 3043 base oil. The Nexbase 3030 and 3043 base oils are 3.0 and 4.3 mm²/s oils, respectively. The physically blended F-ROMP also had 6.5 wt.% Anglamol additive, like the original five fluids. The polymer in F-ROMP is neither linear like PIB and BDIP nor branched like PAO, MABD, and PAMD. The degree of branching in ROMP polymer is in between of these two sets of polymers. The number average molecular weight and polydispersity index of ROMP polymer were 10 kg/mol and 1.5, respectively. The measured kinematic viscosity of F-ROMP was 5.6 mm²/s and 25.5 mm²/s at 100 and 40 °C, respectively. VI, TE, and TC were measured using experimental data for this fluid (values in the Supporting Information).
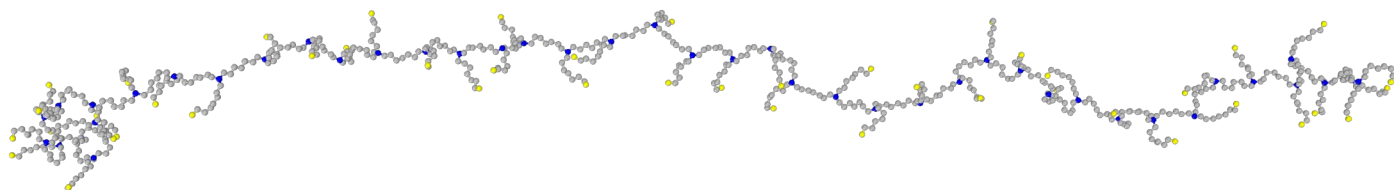

Figure 12. Structure of ROMP polymer in the F-ROMP fluid. The sphere colors represent the following pseudoatoms: yellow-CH_3, silver-CH_2, and blue-CH.

Next, the new fluid was created in the simulations. Since we did not know the chemistry of the Nexbase oils, we replaced Nexbase 3.0 cSt with the previously formulated PAO 3.0 cSt (see Table S3) and Nexbase 4.3 cSt with a newly identified blend of 84.3 wt.% of PAO 4 cSt and 15.7 wt.% of PAO 8 cSt (the viscosity of this blend of PAO 4 cSt and PAO 8 cSt is 4.28 cSt at 100°C = PAO4.3). The resultant PAO base oil has the same viscosity as the blend of Nexbase base oils. Therefore, the F-ROMP fluid model was virtually modeled in Material Studio software by mixing 5.8 wt.% of F-ROMP polymer, 51.7 wt.% of PAO3, and 42.5 wt.% of PAO4.3. Simulations were run with the new fluid to calculate the 17 structural parameters used in the simple models at 40 and 100 °C.

The VI of F-ROMP was calculated using Equation (5), TE was calculated using Equation (7), and TC was calculated using Equation (10) with the fit parameters in Table 2. The model predicted VI and TE are compared to experimentally measured data in Figures 15(a) and 15(b). As expected, the model predictions are very accurate, particularly the trends and magnitudes, for the five fluids used to fit the model parameters. For the F-ROMP, the model predicted TE very accurately and only slightly overpredicts VI. Importantly, the model accurately predicts the relative position of F-ROMP in the increasing VI trend. For TE, the model predicted both the trend and absolute value of TE for all the fluids well, including the test fluid F-ROMP. This degree of matching is impressive since the models were developed for a different base oil than used in the F-ROMP formulation.
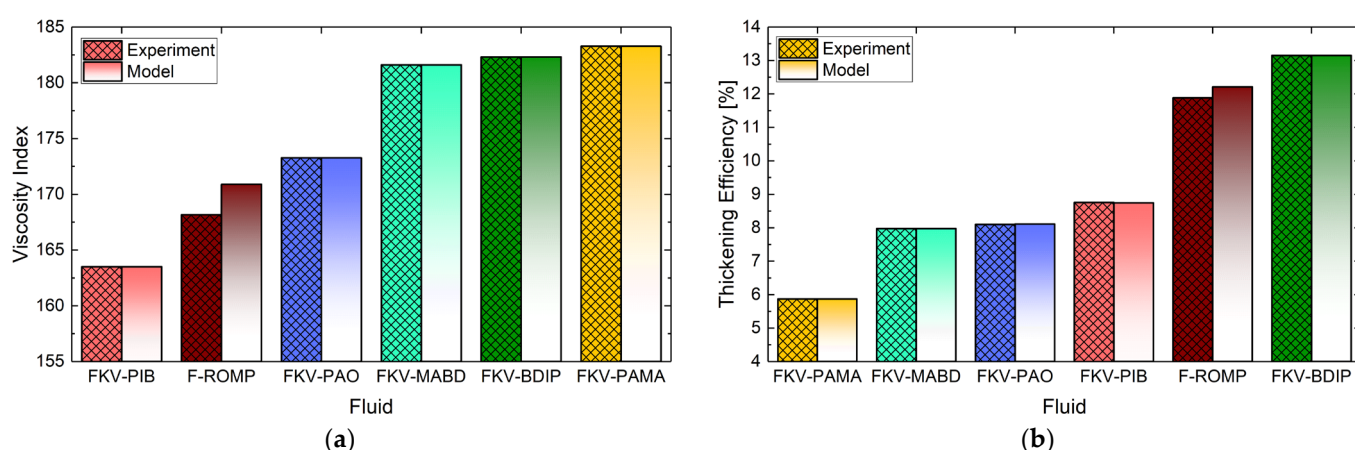

Figure 13. (a) VI and (b) TE at 100 °C for all fluids, including new test fluid F-ROMP, from experiments (patterned bars) and the empirical models fit to just the first five fluids (bars with white-to-solid gradient).

The simulated TC data and extrapolated traction curve for F-ROMP are reported in the supplementary document Section S12. The TCs from simulation, experiment, and predicted by Model C at a range of shear rates are shown in Figure 14(a). In this figure, the blue dashed line is a perfect fit, and the blue and red asterisks are the TC for the five original fluids and F-ROMP, respectively, both from the experiments and simulations. To compare the model-predicted TC to experimental values, the original five fluids were simulated at shear rate consistent to MTM test conditions, that is

1.6×10^6 1/s, whereas the F-ROMP was simulated at shear rate of 1.9×10^6 1/s. Then, using the coordinates of the atoms, the polymer properties in Model C were calculated to predict TC at the experimental shear rate. The results are shown in Figure 14(b). While the model accurately predicts the trend of the original five fluids and magnitude of the test fluid F-ROMP, it does not correctly place the test fluid F-ROMP in the increasing TC trend. This error may be due to inaccuracies in estimation of the MTM shear rate, the non-linearity of the TC with shear rate, the difference between the experimental and simulated film thickness, as well as, for F-ROMP, the difference in the simulated and actual base oil. However, the accuracy of the TC model is still impressive and, notably, the model can predict TC over wide range of shear rates since it was developed from experimental TCs at 1.6×10^6 and simulated TCs at shear rates between 1×10^7 and 1×10^{11} 1/s.
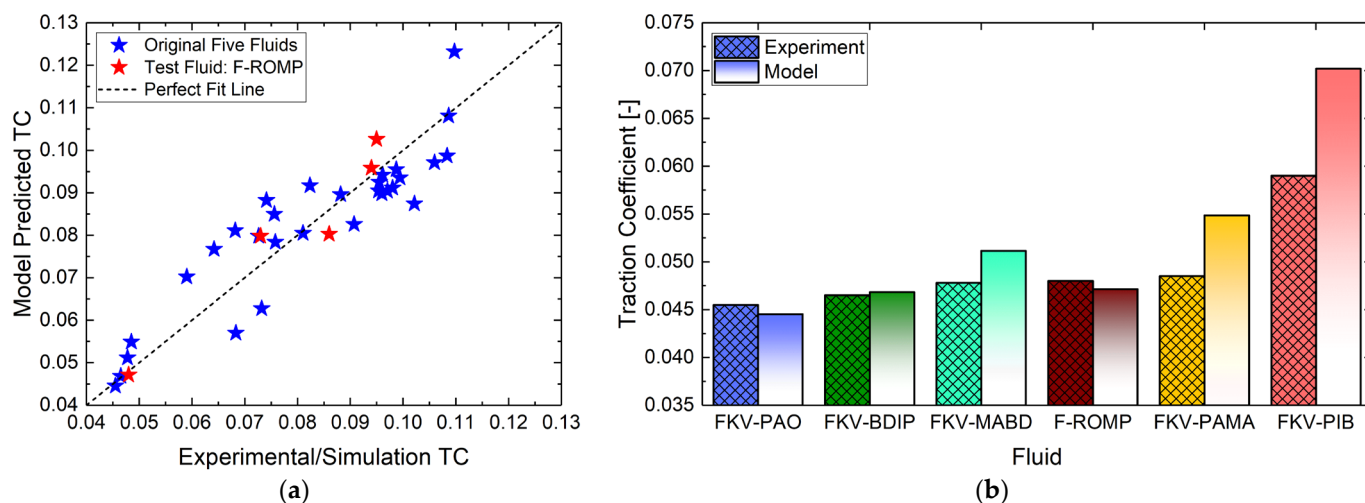

Figure 14. (a) Model predicted traction coefficients for all fluids at high shear rates to directly compare to simulation calculated. The blue dashed line is a perfect fit line, blue asterisks represent simulation-calculated TC for the five fluids used to develop the model and red asterisks represent the TC predicted using model and the simulation data for the test fluid F-ROMP. (b) TE at 40 °C for all fluids, including new test fluid F-ROMP, from experiments (patterned bars) and the empirical models fit to just the first five fluids (bars with white-to-solid gradient).

4. Conclusions

In this study, MD simulations, experimental measurements, and empirical modeling were used to study the effect of chemistry and structure of polymers on three lubricant performance metrics. Five fluids of similar viscosity were formulated with PAO, PIB, BDIP, PAMA, and MABD polymers in PAO base oil of 3 mm²/s. These polymers cover a broad range of molecular weight, chemistry, and degree of branching. Both kinematic and dynamic viscosity were measured using a viscosimeter and a rheometer at 40 and 100 °C, and the VI and TE calculated. The TC was measured using an MTM. The measured data was then used to validate the MD simulations. For the viscosity simulations, various simulation parameters were optimized and the dependency of viscosity simulation approach on correlation length, simulation time, number of trajectories were investigated. Both the kinematic and dynamic viscosity of fluid at both temperatures were in very good agreement with the experimental data. Then, an accurate and computationally efficient approach was presented to simulate TC. In this approach, the confined molecules were sheared by directly deforming the simulation box instead of modeling solid surfaces. The computational efficiency and accuracy of the method were demonstrated here, although further assessment is required to assess the influence of system size and aspect ratio. A simple approach was also presented to extrapolate simulated traction data to experimentally accessible shear rates. The resultant TCs were slightly higher than experimental values, but the trends were consistent.

Comparing the different fluid formulations, the following trends were observed:
- VI: FKV-PIB < FKV-PAO < FKV-MABD < FKV-BDIP < FKV-PAMA,
- TE: FKV-PAMA < FKV-MABD < FKV-PAO < FKV-PIB < FKV-BDIP,
- TC: FKV-PAO < FKV-BDIP < FKV-MABD < FKV-PAMA < FKV-PIB.

From this, was concluded that the branched polymers provided higher VI, while linear and longer polymer provided higher TE. However, the dependence of TC on branching was not clear. For example, PIB is both more linear and smaller

than the other polymers but still had the highest TC, whereas PAO is both small and branched but provided the lowest TC amongst all the polymers. The difference in TC was not clear, it could also be since the difference in chemistries of PAO, BDIP, PAMA, and MABD is comparatively small. The difference in VI, TE, and TC of the fluids were studied in terms of the two most used structural parameters, percentage molecular weight of the polymer in backbone and radius of gyration of the polymer. This investigation showed that VI is somewhat correlated to radius of gyration and TE is highly correlated to the percentage of molecular weight in the backbone of the polymer. However, TC was very weakly correlated with either of structural parameters. Further, although some correlations were observed, neither parameter could capture all trends exhibited by the five fluids studied here. Therefore, to capture the effects of multiple molecular parameters, we used the simplest machine learning tool possible, i.e., multiple linear regression.

To quantify the molecular origins of the VI, TE, and TC, 22 different structural parameters were calculated, including five properties from various molecular weights based on chemistry and 17 properties from the positions of atoms in the MD simulations. Empirical models were developed based on these parameters. It was found that better models, i.e., more accurate predictions, could be achieved using the simulation properties. The best models were evaluated by comparing their predictions to experimental data for a fluid not included in the model development. The models accurately predicted both the magnitude and trend of VI and TE for all the fluids, including the test fluid that was not used in model development. The TC model accurately predicted the trend of all fluids except the test fluid and accurately predicted the magnitude of the test fluid TC. The limitations of the model are primarily attributed to the fact that only five fluids were included in the parameterization and that the test fluid had a different base oil than that of the fluids used in model development. The next step could be to expand the data set and further develop the mathematical models to correlate dynamic descriptors from the simulations to lubricant performance metrics.

Overall, we have demonstrated use of molecular simulations to accurately predict VI, TE, and TC of lubricant formulations with commercial relevance. We further used the simulations to develop empirical models based on properties that could be calculated using relatively short simulations. Adding more data to the models, e.g., different polymer concentration, different base oil, etc. would make the model more accurate. Ultimately, we believe this can be an approach to accurate prediction of structure-property-function relationship that can guide design of new lubricants or additives.

Supplementary Materials: The following are available in the supplementary document, Figure S1: Schematics of (a) Cannon Stress-Tech HR Oscillatory Rheometer and (b) PCS Mini-Traction Machine [1] used for measuring dynamic viscosity and traction coefficient, respectively, Figure S2: (a) Average increase in viscosity of the fluids when the fluids are formulated with 6.5 wt.% of Anglamol 99 additive package compared to the fluids formulated without the additive package. (b) Thickening efficiency calculated from experimentally measured viscosity of the fluids formulated with and without 6.5 wt.% of Anglamol additives package at 100°C, and from the simulation calculated viscosity of the fluids formulated without 6.5 wt.% of Anglamol additives package at 100°C, Figure S3: (a) Experimentally measured kinematic viscosity of the fluids formulated with and without 6.5 wt.% of Anglamol additives package at 40 and 100°C. (b) Experimentally measured traction coefficient of the fluids formulated with and without 6.5 wt.% of Anglamol additives package at 40°C, Figure S4: Simulation box, Figure S5: Optimization of simulation parameters for forcefield, Figure S6: Dependence of viscosity on simulation parameters, Figure S7: Average viscosity and standard deviation plots of all fluids, Figure S8: Traction coefficients calculated from the linear fit of the shear stress to the normal pressure, and the extrapolated traction curve of each fluid, Figure S9: Avg. viscosity and traction curve of F-ROMP fluid, Table S1: Experimental and simulated viscosities at 40 and 100 °C of all fluids, Table S2: Experimental and simulated traction coefficient of test fluids, Table S3: Properties of 3 cSt PAO base oil blend, Table S4. Calculation of ratio of base oil molecules in the proposed 3 cSt PAO base oil, Table S5: Simulation plans Table S6: UA force field parameters for non-bonded interactions, Table 7: UA force field parameters for 1–2 bonded interactions, Table S8: UA force field parameters for 1–3 bonded interactions, Table S9: UA force field parameters for 1–4 bonded interactions, Table S10: Structural parameters used in modeling VI and TE, Table S11: Structural parameters used in modeling TC, Table S12: Composition of F-ROMP fluid, Table S13: Measured and simulated properties of F-ROMP fluid.

Conflicts of Interest: The authors declare no conflicts of interest.

Abbreviations

BDIP	butadiene isoprene
EMD	equilibrium molecular dynamics
GK	Green–Kubo
MABD	methacrylate butadiene
MD	molecular dynamics
NPT	isothermal–isobaric ensemble
NVE	canonical ensemble
NVT	microcanonical ensemble
PIB	polyalphaolefin
PAMA	polyalkyl methacrylate
PAO	polyalphaolefin
PAO2	polyalphaolefin of 2 mm^2/s at 100 °C
PAO3	polyalphaolefin of 3 mm^2/s at 100 °C
PAO4	polyalphaolefin of 4 mm^2/s at 100 °C
PAO8	polyalphaolefin of 8 mm^2/s at 100 °C
PAO4.3	polyalphaolefin of 4.3 mm^2/s at 100 °C
TC	Traction coefficient
TE	thickening efficiency
TraPPE	transferable potentials for phase equilibria
UA	united atom
VI	viscosity index
VIF	variance inflation factor
VM	viscosity modifier

Nomenclature

b	asphericity
c	acylindricity
C	concentration of polymer
k	relative shape anisotropy
k_B	Boltzmann constant
L_x, L_y, L_z	molecules length in $x, y,$ and z direction
M_w	mass average molar mass of polymer
M_n	number average molar mass of polymer
M_{wt}	total molar mass or molecular weight of polymer
M_{wp}	percentage molecular weight of polymer in backbone
M_{wb}	molecular weight of backbone

R	end-to-end distance
R_g	radius of gyration
$R_{g,xx}^2$, $R_{g,yy}^2$, $R_{g,zz}^2$	diagonal elements of gyration tensor
$R_{g,xy}^2$, $R_{g,xz}^2$, $R_{g,yz}^2$	off-diagonal elements of gyration tensor
$P_{\alpha\beta}$	pressure or stress tensor
T	temperature
V	volume
η_{0s}	Newtonian viscosity of fluid
η_{0B}	Newtonian viscosity of base oil
ρ	mass density
ρ_p	density of polymer
ρ_B	density of solvent or base oil
λ_x, λ_y, λ_z	eigen values/principal moments of gyration tensor

References

[1]   Strate, G. Ver, 1991, "Polymers as Lubricating-Oil Viscosity Modifiers," pp. 256–272.

[2]   Covitch, M. J., and Trickett, K. J., 2015, "How Polymers Behave as Viscosity Index Improvers in Lubricating Oils," Adv. Chem. Eng. Sci.

[3]   Gold, P. W., Schmidt, A., Dicke, H., Loos, J., and Assmann, C., 2001, "Viscosity-Pressure-Temperature Behaviour of Mineral and Synthetic Oils," J. Synth. Lubr., **18**(1), pp. 51–79.

[4]   Wong, V. W., and Tung, S. C., 2018, "Friction, Lubrication, and Wear of Internal Combustion Engine Parts," Frict. Lubr. Wear Technol., **18**, pp. 899–915.

[5]   Moughon, L., and Wong, V. W., 2005, "Effects of Lubricant and Piston Design on Reciprocating Engine Friction," *2005 Fall Technical Conference of the ASME Internal Combustion Engine Division*, pp. 653–662.

[6]   ASTM D2270, 2016, "Standard Practice for Calculating Viscosity Index from Kinematic Viscosity at 40 °C and 100 °C," ASTM Int.

[7]   Stöhr, T., Eisenberg, B., and Müller, M., 2009, "A New Generation of High Performance Viscosity Modifiers Based on Comb Polymers," SAE Int. J. Fuels Lubr., **1**(1), pp. 1511–1516.

[8]   Glass, J. E., Schulz, D. N., and Zukoski, C. F., 1991, *Polymers as Rheology Modifiers*, American Chemical Society, Washington.

[9]   Bercea, M., Bercea, I., Nélias, D., and Flamand, L., 2002, "Polyethylene as an Additive for Mineral Oils- Part II: EHL Traction Behavior," Tribol. Trans., **45**(2), pp. 145–152.

[10]   Wang, Y. S., Yang, B. Y., and Wang, L. Q., 2004, "Investigation into the Traction Coefficient in Elastohydrodynamic Lubrication," *TriboTest*, pp. 113–124.

[11]   Sullivan, W. T., Oumar-Mahamat, H., Webster, M. N., and Brandes, E. B., 2010, "Lubricating Fluids with Low Traction Characteristics."

[12]   Miller, M. K., Khalid, H., Michael, P. W., Guevremont, J. M., Garelick, K. J., Pollard, G. W., Whitworth, A. J., and Devlin, M. T., 2014, "An Investigation of Hydraulic Motor Efficiency and Tribological Surface Properties," Tribol. Trans., **57**(4), pp. 622–630.

[13]   Michael, P. W., Mettakadapa, S., and Shahahmadi, S., 2016, "An Adsorption Model for Hydraulic Motor Lubrication," J. Tribol., **138**(1).

[14]   Michael, P. W., and Mettakadapa, S., 2016, "Bulk Modulus and Traction Effects in an Axial Piston Pump and a Radial Piston Motor," 10th Int. Fluid Power Conf., pp. 301–312.

[15]   GOI, T., TANAKA, H., NAKASHIMA, K., and WATANABE, K., 2010, "Study on Stability of High Speed Traction Drive CVT for Aircraft Generator," J. Japan Soc. Aeronaut. Sp. Sci., **58**(678), pp. 203–209.

[16]   Bell, D D, Raynard, A. E., 1980, "Design Study of Toroidal Traction Cvt for Electric Vehicles."

[17]   Balakin, P. D., and Stripling, L. O., 2017, "Power and Energy Ratios in Mechanical CVT Drive Control," J. Phys. Conf. Ser., **858**(1).

[18]   LaFountain, A., Johnston, G. J., and Spikes, H. A., 1998, "Elastohydrodynamic Friction Behavior of Polyalphaolefin Blends," Tribol. Ser., **34**, pp. 465–475.

[19]   Len, M., Ramasamy, U. S., Lichter, S., and Martini, A., 2018, "Thickening Mechanisms of Polyisobutylene in Polyalphaolefin," Tribol. Lett., **66**(1).

[20]   Cosimbescu, L., Vellore, A., Ramasamy, U. S., Burgess, S. A., and Martini, A., 2018, "Low Molecular Weight Polymethacrylates as Multi-Functional Lubricant Additives," Eur. Polym. J., **104**, pp. 39–44.

[21]   Canter, N., 2011, "Viscosity Index Improvers," Tribol. Lubr. Technol., **67**(9), pp. 10–22.

[22]   Cai, G., Zhang, L., Ma, L., and Eli, W., 2015, "Synthesis and Characterization of Polybutylacrylate Viscosity Index Improver with Anti-Wear Function," Lubr. Sci., **27**(4), pp. 209–216.

[23]   Stachowiak, G., and Batchelor, A., 2006, *Engineering Tribology*, Burlington.

[24]   Rizvi, S. Q. A., 2020, *A Comprehensive Review of Lubricant Chemistry , Technology , Selection , A Comprehensive Review of Lubricant Chemistry , Technology , Selection , And*.

[25]   Ahmed, N. S., and Nassar, A. M., 2011, *Lubricating Oil Additives*, Open Access Publisher.

[26]   Ramasamy, U. S., Cosimbescu, L., and Martini, A., 2015, "Temperature-Dependent Conformations of Model Viscosity Index Improvers," Tribol. Lubr. Technol., **71**(5), pp. 30–31.

[27]   Martini, A., Ramasamy, U. S., and Len, M., 2018, "Review of Viscosity Modifier Lubricant Additives," Tribol. Lett., **66**(2).

[28]   Ramasamy, U. S., Lichter, S., and Martini, A., 2016, "Effect of Molecular-Scale Features on the Polymer Coil Size of Model Viscosity Index Improvers," Tribol. Lett., **62**(2), pp. 1–7.

[29]   Bhushan, B., 2000, *Modern Tribology Handbook, Two Volume Set*, CRC Press, Boca Raton.

[30]   Jukic, A., Vidovic, E., and Janovic, Z., 2007, "Alkyl Methacrylate and Styrene Terpolymers as Lubricating Oil Viscosity Index Improvers," Chem. Technol. Fuels Oils, **43**(5), pp. 386–394.

[31]   Mohamad, S. A., Ahmed, N. S., Hassanein, S. M., and Rashad, A. M., 2012, "Investigation of Polyacrylates Copolymers as Lube Oil Viscosity Index Improvers," J. Pet. Sci. Eng., **100**, pp. 173–177.

[32]   Šoljić Jerbić, I., Parlov Vuković, J., and Jukić, A., 2012, "Production and Application Properties of Dispersive Viscosity Index Improvers," Ind. Eng. Chem. Res., **51**(37), pp. 11914–11923.

[33]   Wang, J., Ye, Z., and Zhu, S., 2007, "Topology-Engineered Hyperbranched High-Molecular-Weight Polyethylenes as Lubricant Viscosity-Index Improvers of High Shear Stability," pp. 1174–1178.

[34]   Morgan, S., Ye, Z., Subramanian, R., and Zhu, S., 2010, "Higher-Molecular-Weight Hyperbranched Polyethylenes Containing Crosslinking Structures as Lubricant Viscosity-Index Improvers," Polym. Eng. Sci., **50**(5), pp. 911–918.

[35]   Nunez, C. M., Chiou, B. Sen, Andrady, A. L., and Khan, S. A., 2000, "Solution Rheology of Hyperbranched Polyesters and Their Blends with Linear Polymers," Macromolecules, **33**(5), pp. 1720–1726.

[36]   Knothe, G., and Steidley, K. R., 2005, "Kinematic Viscosity of Biodiesel Fuel Components and Related Compounds. Influence of Compound Structure and Comparison to Petrodiesel Fuel Components," Fuel, **84**(9), pp. 1059–1065.

[37]   Gaciño, F. M., Regueira, T., Lugo, L., Comuñas, M. J. P., and Fernández, J., 2011, "Influence of Molecular Structure on Densities and Viscosities of Several Ionic Liquids," J. Chem. Eng. Data, **56**(12), pp. 4984–4999.

[38]   Bhattacharya, P., Ramasamy, U. S., Krueger, S., Robinson, J. W., Tarasevich, B. J., Martini, A., and Cosimbescu, L., 2016, "Trends in Thermoresponsive Behavior of Lipophilic Polymers," Ind. Eng. Chem. Res., **55**(51), pp. 12983–12990.

[39]   Van Ravensteijn, B. G. P., Bou Zerdan, R., Seo, D., Cadirov, N., Watanabe, T., Gerbec, J. A., Hawker, C. J., Israelachvili, J. N., and Helgeson, M. E., 2019, "Triple Function Lubricant Additives Based on Organic-Inorganic Hybrid Star Polymers: Friction Reduction, Wear Protection, and Viscosity Modification," ACS Appl. Mater. Interfaces, **11**(1), pp. 1363–1375.

[40]   Panwar, P., Len, M., Gajghate, N., Michael, P., and Martini, A., 2020, "Fluid Effects on Mechanical Efficiency of Hydraulic

Pumps: Dynamometer Measurements and Molecular Simulations," ASME/BATH 2019 Symp. Fluid Power Motion Control. FPMC 2019.

[41] Kioupis, L. I., and Maginn, E. J., 1999, "Molecular Simulation of Poly-α-Olefin Synthetic Lubricants: Impact of Molecular Architecture on Performance Properties," J. Phys. Chem. B, **103**(49), pp. 10781–10790.

[42] Khabaz, F., and Khare, R., 2014, "Effect of Chain Architecture on the Size, Shape, and Intrinsic Viscosity of Chains in Polymer Solutions: A Molecular Simulation Study," J. Chem. Phys., **141**(21).

[43] Ramasamy, U. S., Lichter, S., and Martini, A., 2016, "Effect of Molecular-Scale Features on the Polymer Coil Size of Model Viscosity Index Improvers," Tribol. Lett., **62**(2).

[44] Ramasamy, U. S., Len, M., and Martini, A., 2017, "Correlating Molecular Structure to the Behavior of Linear Styrene–Butadiene Viscosity Modifiers," Tribol. Lett., **65**(4).

[45] Panwar, P., Michael, P., Devlin, M., and Martini, A., 2020, "Critical Shear Rate of Polymer-Enhanced Hydraulic Fluids," Lubricants, **8**(12), pp. 1–15.

[46] Selby, T. W., 1958, "The Non-Newtonian Characteristics of Lubricating Oils," ASLE Trans.

[47] Berry, G. C., 1988, "Remarks on a Relation among the Intrinsic Viscosity, the Radius of Gyration, and the Translational Friction Coefficient," J. Polym. Sci. Part B Polym. Phys., **26**(5), pp. 1137–1142.

[48] Farmer, B. S., Terao, K., and Mays, J. W., 2006, "Characterization of Model Branched Polymers by Multi-Detector SEC in Good and Theta Solvents," Int. J. Polym. Anal. Charact., **11**(1), pp. 3–19.

[49] Nassar, A. M., 2008, "Synthesis and Evaluation of Viscosity Index Improvers and Pour Point Depressant for Lube Oil," Pet. Sci. Technol., **26**(5), pp. 523–531.

[50] Ghosh, P., and Das, M., 2014, "Study of the Influence of Some Polymeric Additives as Viscosity Index Improvers and Pour Point Depressants - Synthesis and Characterization," J. Pet. Sci. Eng., **119**, pp. 79–84.

[51] Mary, C., Philippon, D., Lafarge, L., Laurent, D., Rondelez, F., Bair, S., and Vergne, P., 2013, "New Insight into the Relationship between Molecular Effects and the Rheological Behavior of Polymer-Thickened Lubricants under High Pressure," Tribol. Lett.

[52] LaRiviere, D., Asfour, A. F. A., Hage, A., and Gao, J. Z., 2000, "Viscometric Properties of Viscosity Index Improvers in Lubricant Base Oil over a Wide Temperature Range. Part I: Group II Base Oil," Lubr. Sci., **12**(2), pp. 133–143.

[53] Mueller, H. G., 1978, "Mechanism of Action of Viscosity Index Improvers," Tribol. Int., (June), pp. 189–192.

[54] Rizvi, S. Q. A., 2009, *A Comprehensive Review of Lubricant Chemistry, Technology, Selection, and Design*, ASTM International, Conshohocken.

[55] Radke, W., and Müller, A. H. E., 2005, "Synthesis and Characterization of Comb-Shaped Polymers by SEC with on-Line Light Scattering and Viscometry Detection," Macromolecules, **38**(9), pp. 3949–3960.

[56] Lashkhi, V. L., and Fuks, I. G., 1988, "Polymer-Compounded Oils. Properties and Specific Features of Application," Chem. Technol. Fuels Oils, **24**(11), pp. 492–498.

[57] Cecil, R., Pike, W. C., and Raje, N. R., 1973, "Development of Methods for Evaluating Traction Fluids," Wear, **26**(3), pp. 335–353.

[58] Haseltine, M. W., Duling, I. N., Hagstrom, P. E., Stenger, R. J., and Gates, D. S., 1971, "Design and Development of Fluids for Traction and Friction Type Transmissions," SAE Tech. Pap.

[59] Muraki, M., 1987, "Molecular Structure of Synthetic Hydrocarbon Oils and Their Rheological Properties Governing Traction Characteristics," Tribol. Int., **20**(6), pp. 347–354.

[60] Kyotani, T., Yoshitake, H., Ito, T., and Tamai, Y., 1986, "Correlation between Flow Properties and Traction of Lubricating Oils," ASLE Trans., **29**(1), pp. 102–106.

[61] Tsubouchi, T., and Hata, H., 1996, "Quantitative Correlations between the Fundamental Molecular Structures and Traction Properties of Traction Fluids," Japanese J. Tribol., **41**(5), pp. 463–474.

[62] Hata, H., and Tsubouchi, T., 1998, "Molecular Structures of Traction Fluids in Relation to Traction Properties," Tribol. Lett.,

5(1), pp. 69–74.

[63]   Tsubouchi, T., and Hata, H., 1995, "Study on the Fundamental Molecular Structures of Synthetic Traction Fluids: Part 2," Tribol. Int., **28**(5), pp. 335–340.

[64]   Dare-Edwards, M. P., 1991, "A Novel Family of Traction Fluids Deriving from Molecular Design," J. Synth. Lubr., **8**(3), pp. 197–205.

[65]   Tsubouchi, T., Abe, K., and Hata, H., 1993, "Quantitative Correlation between Molecular Structures of Traction Fluids and Their Traction Properties (Part 1): Influence of Alkylene Chain," Japanese J. Tribol., **38**(3), pp. 403–410.

[66]   Tsubouchi, T., and Shinoda, J., 2009, "Characterization of Oily High Bulk Modulus Fluid," World Tribol. Congr. 2009 - Proc., p. 532.

[67]   Yamano, H., Shiota, K., Miura, R., Katagiri, M., Kubo, M., Stirling, A., Broclawik, E., Miyamoto, A., and Tsubouchi, T., 1996, "Molecular Dynamics Simulation of Traction Fluid Molecules under EHL Condition," Thin Solid Films, **281–282**(1–2), pp. 598–601.

[68]   Washizu, H., Sanda, S., Hyodo, S., Ohmori, T., Nishino, N., and Suzuki, A., 2007, "A Molecular Dynamics Analysis of the Traction Fluids," SAE Tech. Pap.

[69]   Lu, J., Wang, Q. J., Ren, N., and Lockwood, F. E., 2019, "Correlation between Pressure-Viscosity Coefficient and Traction Coefficient of the Base Stocks in Traction Lubricants: A Molecular Dynamic Approach," Tribol. Int., **134**, pp. 328–334.

[70]   Washizu, H., Ohmori, T., and Suzuki, A., 2017, "Molecular Origin of Limiting Shear Stress of Elastohydrodynamic Lubrication Oil Film Studied by Molecular Dynamics," arXiv.

[71]   Gattinoni, C., Heyes, D. M., Lorenz, C. D., and Dini, D., 2013, "Traction and Nonequilibrium Phase Behavior of Confined Sheared Liquids at High Pressure," Phys. Rev. E - Stat. Nonlinear, Soft Matter Phys., **88**(5).

[72]   ASTM D445-18, 2010, "Standard Test Method for Kinematic Viscosity of Transparent and Opaque Liquids (and Calculation of Dynamic Viscosity)," Annu. B. ASTM Stand.

[73]   Nichetti, D., and Manas-Zloczower, I., 1998, "Viscosity Model for Polydisperse Polymer Melts," J. Rheol. (N. Y. N. Y)., **42**(4), pp. 951–969.

[74]   Grandelli, H. E., Dickmann, J. S., Devlin, M. T., Hassler, J. C., and Kiran, E., 2013, "Volumetric Properties and Internal Pressure of Poly(α-Olefin) Base Oils," Ind. Eng. Chem. Res., **52**(50), pp. 17725–17734.

[75]   Brown, S. F., 2015, "Base Oil Groups: Manufacture, Properties, and Performance," Tribol. Lubr. Technol., **71**(4), pp. 32–35.

[76]   Gartner, T. E., and Jayaraman, A., 2019, "Modeling and Simulations of Polymers: A Roadmap," Macromolecules, **52**(3), pp. 755–786.

[77]   Yeh, I. C., and Hummer, G., 2004, "System-Size Dependence of Diffusion Coefficients and Viscosities from Molecular Dynamics Simulations with Periodic Boundary Conditions," J. Phys. Chem. B, **108**(40), pp. 15873–15879.

[78]   Landau, L. D., Lifshitz, E. M., and Reichl, L. E., 1981, "Statistical Physics, Part 1," Phys. Today, **31**(1).

[79]   Robbins, M. O., Grest, G. S., and Kremer, K., 1990, "Effect of Finite System Size on Thermal Fluctuations: Implications for Melting," Phys. Rev. B, **42**(9), pp. 5579–5585.

[80]   Bair, S., McCabe, C., McCabe, C., Cummings, P. T., and Cummings, P. T., 2002, "Comparison of Nonequilibrium Molecular Dynamics with Experimental Measurements in the Nonlinear Shear-Thinning Regime," Phys. Rev. Lett., **88**(5), pp. 583021–583024.

[81]   Mondello, M., and Grest, G. S., 2002, "Viscosity Calculations of n -Alkanes by Equilibrium Molecular Dynamics Viscosity Calculations of n-Alkanes by Equilibrium Molecular Dynamics," **9327**(March 1997).

[82]   Mondello, M., Grest, G. S., Webb, E. B., and Peczak, P., 1998, "Dynamics of N-Alkanes: Comparison to Rouse Model," J. Chem. Phys., **109**(2), pp. 798–805.

[83]   Mondello, M., Grest, G. S., Mondello, M., and Grest, G. S., 1998, "Molecular Dynamics of Linear and Branched Alkanes Molecular Dynamics of Linear and Branched Alkanes," **7156**(June 1995).

[84]   Ewen, J. P., Gattinoni, C., Thakkar, F. M., Morgan, N., Spikes, H. A., and Dini, D., 2016, "A Comparison of Classical Force-

Fields for Molecular Dynamics Simulations of Lubricants," Materials (Basel)., **9**(8), pp. 1–17.

[85]   Jadhao, V., and Robbins, M. O., 2019, "Rheological Properties of Liquids Under Conditions of Elastohydrodynamic Lubrication," Tribol. Lett.

[86]   Robbins, M. O., 2017, "Probing Large Viscosities in Glass-Formers with Nonequilibrium Simulations," **114**(39), pp. 7952–7957.

[87]   Yang, T., Sun, Y., Meng, X., Wu, J., and Ilja Siepmann, J., 2021, "Simultaneous Measurement of the Density and Viscosity for N-Decane + CO2 Binary Mixtures at Temperature between (303.15 to 373.15) K and Pressures up to 80 MPa," J. Mol. Liq., **338**.

[88]   Martin, M. G., and Siepmann, J. I., 1998, "Transferable Potentials for Phase Equilibria. 1. United-Atom Description of n-Alkanes," J. Phys. Chem. B, **102**(14), pp. 2569–2577.

[89]   Martin, M. G., and Siepmann, J. I., 1999, "Novel Configurational-Bias Monte Carlo Method for Branched Molecules. Transferable Potentials for Phase Equilibria. 2. United-Atom Description of Branched Alkanes," J. Phys. Chem. B, **103**(21), pp. 4508–4517.

[90]   Ferrando, N., Gedik, I., Lachet, V., Pigeon, L., and Lugo, R., 2013, "Prediction of Phase Equilibrium and Hydration Free Energy of Carboxylic Acids by Monte Carlo Simulations," J. Phys. Chem. B, **117**(23), pp. 7123–7132.

[91]   Clifford, S., Bolton, K., and Ramjugernath, D., 2006, "Monte Carlo Simulation of Carboxylic Acid Phase Equilibria," J. Phys. Chem. B, **110**(43), pp. 21938–21943.

[92]   Wick, C. D., Martin, M. G., and Siepmann, J. I., 2000, "Transferable Potentials for Phase Equilibria. 4. United-Atom Description of Linear and Branched Alkenes and Alkylbenzenes," J. Phys. Chem. B, **104**(33), pp. 8008–8016.

[93]   Chen, B., Potoff, J. J., and Siepmann, J. I., 2002, "Monte Carlo Calculations for Alcohols and Their Mixtures with Alkanes. Transferable Potentials for Phase Equilibria. 5. United-Atom Description of Primary, Secondary, and Tertiary Alcohols," J. Phys. Chem. B, **105**(15), pp. 3093–3104.

[94]   Stubbs, J. M., Potoff, J. J., and Siepmann, J. I., 2004, "Transferable Potentials for Phase Equilibria. 6. United-Atom Description for Ethers, Glycols, Ketones, and Aldehydes," J. Phys. Chem. B, **108**(45), pp. 17596–17605.

[95]   Kamath, G., Cao, F., and Potoff, J. J., 2004, "An Improved Force Field for the Prediction of the Vapor-Liquid Equilibria for Carboxylic Acids," J. Phys. Chem. B, **108**(37), pp. 14130–14136.

[96]   Kamath, G., Robinson, J., and Potoff, J. J., 2006, "Application of TraPPE-UA Force Field for Determination of Vapor-Liquid Equilibria of Carboxylate Esters," Fluid Phase Equilib., **240**(1), pp. 46–55.

[97]   Maerzke, K. A., Schultz, N. E., Ross, R. B., and Siepmann, J. I., 2009, "TraPPE-UA Force Field for Acrylates and Monte Carlo Simulations for Their Mixtures with Alkanes and Alcohols," J. Phys. Chem. B, **113**(18), pp. 6415–6425.

[98]   Yang, Y., Narayanan Nair, A. K., and Sun, S., 2020, "Sorption and Diffusion of Methane and Carbon Dioxide in Amorphous Poly(Alkyl Acrylates): A Molecular Simulation Study," J. Phys. Chem. B, **124**(7), pp. 1301–1310.

[99]   Dinpajooh, M., and Nitzan, A., 2020, "Heat Conduction in Polymer Chains with Controlled End-to-End Distance," J. Chem. Phys., **153**(16).

[100]   Plimpton, S., 1995, "Fast Parallel Algorithms for Short-Range Molecular Dynamics," J. Comput. Phys., **117**(1), pp. 1–19.

[101]   NosÉ, S., 2002, "A Molecular Dynamics Method for Simulations in the Canonical Ensemble," Mol. Phys., **100**(1), pp. 191–198.

[102]   Hoover, W. G., 1985, "Canonical Dynamics: Equilibrium Phase-Space Distributions," Phys. Rev. A, **31**(3), pp. 1695–1697.

[103]   Maginn, E. J., Messerly, R. A., Carlson, D. J., Roe, D. R., and Elliott, J. R., 2019, "Best Practices for Computing Transport Properties 1. Self-Diffusivity and Viscosity from Equilibrium Molecular Dynamics [Article v1.0]," Living J. Comput. Mol. Sci., **1**(1), pp. 1–20.

[104]   Zhang, Y., Otani, A., and Maginn, E. J., 2015, "Reliable Viscosity Calculation from Equilibrium Molecular Dynamics Simulations: A Time Decomposition Method," J. Chem. Theory Comput., **11**(8), pp. 3537–3546.

[105]   Washizu, H., Sanda, S., Hyodo, S. A., Ohmori, T., Nishino, N., and Suzuki, A., 2008, "All-Atom Molecular Dynamics

Simulation of Submicron Thickness EHL Oil Film," 2007 Proc. ASME/STLE Int. Jt. Tribol. Conf. IJTC 2007, **PART A**, pp. 167–169.

[106] Maćkowiak, S., Heyes, D. M., Dini, D., and Brańka, A. C., 2016, "Non-Equilibrium Phase Behavior and Friction of Confined Molecular Films under Shear: A Non-Equilibrium Molecular Dynamics Study," J. Chem. Phys., **145**(16).

[107] Ewen, J. P., Heyes, D. M., and Dini, D., 2018, "Advances in Nonequilibrium Molecular Dynamics Simulations of Lubricants and Additives," Friction, **6**(4), pp. 349–386.

[108] Todd, B. D., and Daivis, P. J., 2017, *Nonequilibrium Molecular Dynamics: Theory, Algorithms and Applications*, Cambridge University Press.

[109] Bair, S., 2019, *High Pressure Rheology for Quantitative Elastohydrodynamics*, Elsevier.

[110] Han, X. J., and Schober, H. R., 2011, "Transport Properties and Stokes-Einstein Relation in a Computer-Simulated Glass-Forming Cu33.3Zr66.7 Melt," Phys. Rev. B - Condens. Matter Mater. Phys., **83**(22).

[111] Lerner, E., and Bouchbinder, E., 2017, "Effect of Instantaneous and Continuous Quenches on the Density of Vibrational Modes in Model Glasses," Phys. Rev. E, **96**(2).

[112] Shi, J., Wang, J., Yi, X., and Fan, X., 2021, "Effect of Film Thickness on Slip and Traction Performances in Elastohydrodynamic Lubrication by a Molecular Dynamics Simulation," Tribol. Lett., **69**(4).

[113] Bas G. P. van Ravensteijn, Raghida Bou Zerdan, Craig J. Hawker,   and M. E. H., 2021, "Role of Architecture on Thermorheological Properties of Poly(Alkyl Methacrylate)-Based Polymers," Macromolecules, **54**(12), pp. 5473–5483.

[114] Mattice, W. L., and Suter, U. W., 1994, *Conformational Theory of Large Molecules*, Wiley-Interscience, New York.

[115] Theodorou, D. N., and Suter, U. W., 1985, "Shape of Unperturbed Linear Polymers: Polypropylene," Macromolecules, **18**(6), pp. 1206–1214.

[116] Cané, E., Llovell, F., and Vega, L. F., 2017, "Accurate Viscosity Predictions of Linear Polymers from N-Alkanes Data," J. Mol. Liq., **243**, pp. 115–123.